

Similarity and Quality Metrics for MR Image-to-Image Translation

Melanie Dohmen¹, Mark Klemens¹, Ivo Baltruschat¹, Tuan Truong¹, and Matthias Lenga¹

¹Bayer AG, Radiology, Berlin, Germany
firstname.lastname@bayer.com

ABSTRACT

Image-to-image translation can create large impact in medical imaging, as images can be synthetically transformed to other modalities, sequence types, higher resolutions or lower noise levels. To ensure patient safety, these methods should be validated by human readers, which requires a considerable amount of time and costs. Quantitative metrics can effectively complement such studies and provide reproducible and objective assessment of synthetic images. If a reference is available, the similarity of MR images is frequently evaluated by SSIM and PSNR metrics, even though these metrics are not or too sensitive regarding specific distortions. When reference images to compare with are not available, non-reference quality metrics can reliably detect specific distortions, such as blurriness. To provide an overview on distortion sensitivity, we quantitatively analyze 11 similarity (reference) and 12 quality (non-reference) metrics for assessing synthetic images. We additionally include a metric on a downstream segmentation task. We investigate the sensitivity regarding 11 kinds of distortions and typical MR artifacts, and analyze the influence of different normalization methods on each metric and distortion. Finally, we derive recommendations for effective usage of the analyzed similarity and quality metrics for evaluation of image-to-image translation models.

1 Introduction

Recent advances in generative artificial intelligence (AI) within the natural image domain have demonstrated a remarkable capability to produce synthetic images with high fidelity, capturing nuances such as lighting variations, textures, and object placements[1, 2]. The implications of these advancements are far-reaching, with applications spanning various domains such as computer vision, graphics, augmented and virtual reality, or creative arts. Still, many challenges remain, including potential biases in generated images, the need for enhanced diversity and controllability in generation, and ethical considerations surrounding the use of AI-generated content. The adaptation of generative modeling concepts such as Generative Adversarial Networks (GANs)[3] or diffusion models [4, 5] to the medical imaging domain is being explored with continuously growing interest and many relevant use cases have already been identified. For training deep neural networks, typically very large and diverse data sets are needed, but these are rarely available for medical imaging tasks. Generative networks can amend available data with synthetic samples and thereby improve the performance of other image analysis tasks [6]. Another line of research develops conditional generative models for image-to-image translation, which aims to translate a given source image to a synthetic target image, showing the same content (e.g. patient, organ or biological sample) as the source but with a different appearance (e.g. contrasting structures differently, changing texture or resolution). Source and target typically belong to different image domains. Depending on the availability of source and target pairs of the same patient or structure in the training data, image-to-image translation can be performed in a paired[2] or unpaired [7] manner, also referred to as supervised or unsupervised. Image-to-image translation models are trained to transfer characteristics from the target domain to a specific image from the source domain without changing the represented image content. These tasks are specifically interesting in medical applications [8], because they allow to translate a medical image from one domain to another. Source and target domain may differ by imaging modality or acquisition parameters, such that image-to-image translation allows translation, e.g., from computed tomography (CT) to magnetic resonance (MR) imaging [9] or vice-versa [10], from T1-weighted MR to T2-weighted MR [11], CT to positron emission tomography (PET) [12], PET to CT [13], or from native MR to contrast-enhanced MR [14, 15]. There is a significant patient benefit, when the source image can be acquired with less harm, more quickly or at a lower cost, compared to the the target image, which might be preferred for diagnosis. Low-quality or low-resolution images can be restored, improved, or the resolution increased [16]. For radiation therapy, which is planned on the basis of CT images, MR to CT synthesis has been investigated [10]. MR to CT synthesis is also used to facilitate registration between both modalities[17]. The translation between different MR sequences (T1-weighted, T2-weighted, T2-FLAIR) can complete missing series for improved diagnosis [18]. For reducing patient burden with contrast agents, researchers work on the translation of native or low-dose MR images to synthetic high contrast-enhanced images [19].

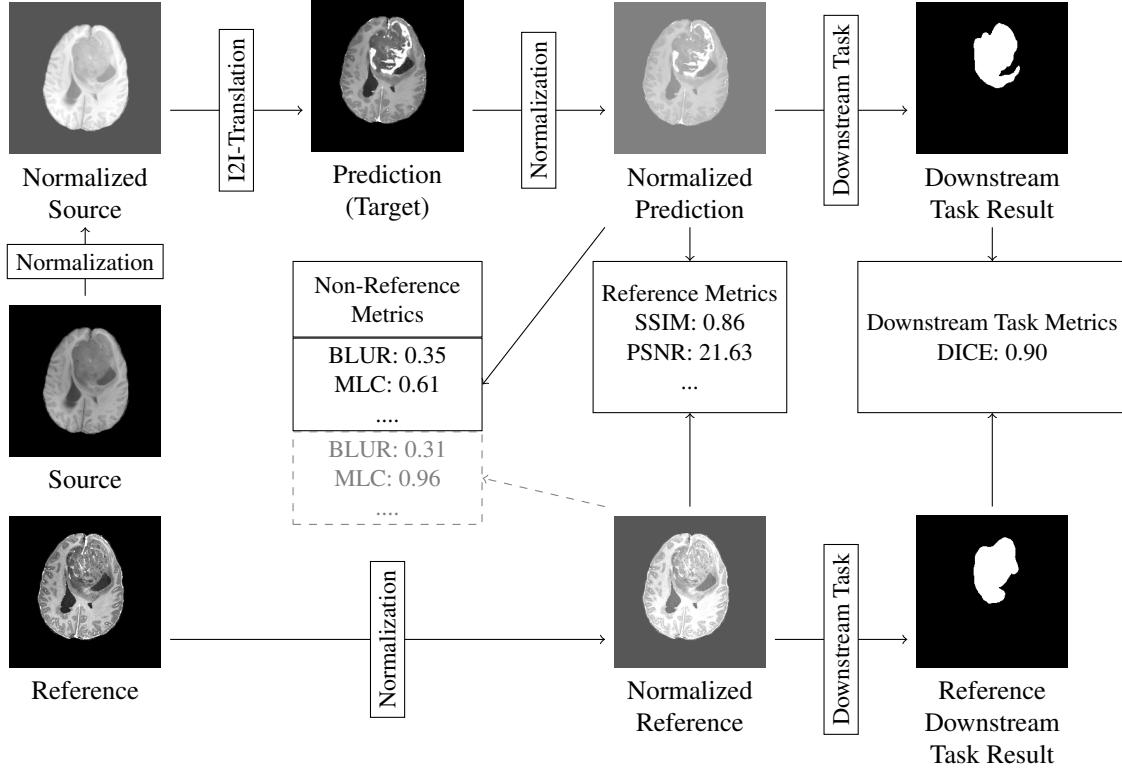


Figure 1. Overview of image-to-image translation and validation. Given a source image, it is typically normalized before being translated to a prediction in the target domain. If a reference image is given, this also belongs to the target domain. To make sure, prediction and reference are comparable, both should be normalized to a common scale. Then there are multiple possibilities to apply metrics. Reference metrics directly compare normalized prediction and normalized reference image. Non-reference metrics can be applied to the normalized prediction alone, but also - if available - to a predicted normalized reference. Then both non-reference metric scores can be compared. Third, the normalized reference and the normalized prediction can be further processed in a downstream task, i.e. a segmentation task. The performance of both downstream task results is then assessed with a downstream task metric, i.e. a segmentation metric.

1.1 Validation Metrics for Image Synthesis

However, validation of these approaches is not straightforward. In addition to manual evaluation by humans, metrics assessing a whole distribution of synthesized images are very popular for evaluating GANs [20], e.g. the Inception Score [21] or the Fréchet Inception Distance [22]. These metrics aim to assess the diversity of the generated images, as well as their coverage and similarity to a reference set of images. Another group called (full-) reference metrics assesses the similarity between two images. In the context of image synthesis, one image is synthesized and it is then compared to a reference image, representing a desired synthesis result. For this validation setup, a dataset with paired source and reference images is needed. Synthesis models leveraging such data are often referred to as paired or supervised image-to-image translation models. Furthermore, there are non-reference metrics or quality metrics, that assess the quality of a single image. As quality requirements may vary between tasks and image domains, metrics for different aspects have been developed, e.g. for measuring blurriness [23], contrast [24], noisiness [25] or other features inspired by human perception [26].

Depending on the application of synthesized images, the evaluation of the images in a downstream task is more appropriate, than the evaluation of the images themselves. The workflow of image-to-image translation and the three types of validation metrics investigated in this study are shown in Fig. 1.

In the domain of natural images, reference metrics have been extensively tested on synthetically distorted images. The Tampere Image Database [27] and the LIVE Image Quality Assessment Database [28, 29] contain 25-29 reference images and differently distorted versions thereof, additionally annotated with a human quality score. Metric scores for various full-reference metrics were correlated with human scores to identify the best performing metrics. However, these results cannot be fully transferred to medical image synthesis. Even though a similar study for MR images [30] exists, the included distortions, such as JPEG compression artifacts and white noise are less relevant for medical image synthesis. Instead, MR imaging, including acquisition

and reconstruction, exhibits very specific artifacts, such as bias field, ghosting or stripe artifacts. Additionally, certain synthesis models may introduce other kinds of distortions, e.g. the insertion of artificial structures or registration artifacts that arise from misaligned source and target images. In this study, we create a similar benchmark dataset for the medical images domain consisting of 100 MR reference images and 11 distortions. Applying the distortions in 5 strengths resulting in comparable quality levels, this allows us to compare different metrics regarding their sensitivity towards each kind of distortion. We consider each distortion by itself instead of averaging over a fixed group of distortions, because the importance and appearance of single distortions may vary largely between different applications.

1.2 Validation in the Medical Domain

Analysis, processing and generation of medical images can have severe impact on patient outcome and patient safety. Therefore, the Food and Drug Administration (FDA) in the United States requires technical and clinical evaluation for every software as a medical device to be approved[31]. Technical validation provides objective evidence, that the software correctly and reliably processes input data and generates output data with the appropriate level of accuracy and reproducibility. Clinical validation measures the ability of a software to yield a clinically meaningful output in the target health care situation. For evaluating medical algorithms based on artificial intelligence, guidelines about trial protocol designs [32] have been agreed on by an expert consortium. However, systemic reviews of published papers on AI-based algorithms in the medical domain have revealed, that only a small fraction of studies adheres to such guidelines, i.e. external validation[33, 34]. Often, details of clinical validation studies, such as test population statistics, are not published, not even for FDA-approved software[35]. Another review found that the median number of health-care professionals engaged in clinical validation was only four [36], which limits the reliability and generizability of such studies. Recent validation studies of FDA approved image-to-image translation software rely strongly on technical assessment of phantom measurements by similarity metrics [37, 38]. While the number of FDA approved medical devices based on AI software is still increasing by 14% (2022), the increase has been slowing down compared to 2020 (39%) [39].

The lack of adequate trials for clinical validation is certainly only one part of the problem. Appropriate technical validation is crucial at an even earlier stage of development. Metrics for biomedical image analysis and segmentation have been extensively described [40, 41], and can be leveraged to indirectly assess synthetic images via downstream tasks [42]. Even though a huge amount of metrics has been used for the evaluation of synthetic medical images [43, 3], to our knowledge guidelines for the selection of appropriate similarity and quality metrics are not available. For validating synthetic MR images, especially structural similarity index measure (SSIM), and peak signal-to-noise ratio (PSNR) are used extensively. A review on image-to-image translation with generative adversarial networks (GANs) or convolutional neural networks (CNNs) in the medical domain [44] reported the use of SSIM in 84% studies and PSNR in 61% studies, that synthesize MR images. A further review on synthetic contrast-enhancement of MR images [45] reports evaluation by SSIM and PSNR in 75% of the studies. This is in opposition to known crucial weak points of SSIM and PSNR, such as underestimated blurriness [46], bad correlation to human perception [47, 48, 49] and difficulties with float-valued images [50, 51]. Therefore, a systematic analysis of appropriate metrics for MR image synthesis validation is needed.

1.3 Contribution

In this paper, we provide a comprehensive overview and description of 11 reference metrics that can be used for the evaluation of synthetic MR images (see Sec. 2). To complement reference metrics and account for applications, where paired reference images are unavailable, we present 12 non-reference metrics and exemplarily discuss the value of downstream task evaluation with a segmentation metric. In the experiments in Sec. 3, we systematically assess the sensitivity of 11 reference and 12 non-reference metrics regarding 11 different distortions, that we assume to appear in MR image synthesis. Furthermore, we use five normalization methods before metric assessment and investigate their influence. Thereby, we aim to guide researchers in the appropriate selection of metrics for any desired synthesis task. After reviewing the distortion experiment results in Sec. 4, we discuss typical shortcomings, but also advantages of certain metrics in Sec. 5. Finally, in Sec. 6, we recommend how to select and best apply metrics for validating image-to-image translation methods specifically for MR image synthesis.

2 Methods

In this section, we give an overview of reference and non-reference metrics for assessing the quality of images. Since most reference and non-reference metrics strongly depend on the intensity value ranges of the images they assess, the examination of metrics must be combined with the examination of normalization methods, that adjust the intensity value ranges. Therefore, we first introduce normalization methods that are frequently used to bring MR images to a common intensity value scale or as prerequisite for certain metrics.

2.1 Intensity Ranges and Data Formats

Image normalization plays a crucial role in medical image processing, serving as a fundamental preprocessing step with significant implications for downstream processing, analysis, or the development of algorithms. Natural images are often stored as RGB images with an 8-bit unsigned integer data format per channel, which corresponds to a value range of $[0, 255]$. Apart from CT images, which are typically stored in Hounsfield Units, the intensity values of medical images such as MR, X-ray or ultra-sound are not standardized. At the same time, medical images may capture more detailed information and, therefore, often exhibit much larger intensity ranges, such as 12- to 16-bit unsigned integer or 32-bit floating point values. Regarding the normalization of intensity ranges for quantitative metric assessment, typically, two problems arise.

First, image intensities are not comparable between two images, due to missing standardization. For example, in MR imaging, the same tissue may be represented by different values depending on scanner, software version or surrounding tissue. In this case, normalization must be applied before metric assessment in order to achieve comparability between two or more images. Normalization or standardization is not only needed as a prerequisite for metric assessment but is usually already performed as a preprocessing step for image-to-image translation models. For deep-learning based methods, a reasonable and standardized scale such as $[-1, 1]$ or $[0, 1]$ is recommended [52]. By modality specific normalization, deep-learning based models may even improve generalizability in case of heterogeneous input data sources [53, 54].

Second, most metrics were designed and developed for 8-bit unsigned integer data format. In most cases, either images need to be normalized into the $[0, 255]$ range, or an additional data range parameter is introduced to adapt to other intensity ranges. For 8-bit images, the data range parameter L is then set to 255, assuming an intensity value range between 0 and 255. For float valued images, the intensity value range is generally infinite, but L should be set to a finite value spanning the range of at least all observed intensity values. Therefore, L is typically set to the difference of maximum and minimum value of an image I ($L_I = I_{\max} - I_{\min}$), or the difference of the joint maximum and minimum of two images I and R ($L_{I,R}$), or of a set of images \mathcal{D} ($L_{\mathcal{D}}$). If $I, R \in \mathcal{D}$, then $L_I \leq L_{I,R} \leq L_{\mathcal{D}}$. It is argued [50], that using $L_{\mathcal{D}}$ results in SSIM values, that do not vary with individual image minimum and maximum values. At least $L_{I,R}$ should be used for reference metrics on two images I and R instead of L_I or L_R , because possibly $L_I \neq L_R$, and then the reference metric would yield different results when interchanging I and R .

2.2 Normalization Methods

Several normalization methods [55], such as Zscore, Minmax or Quantile normalization have been used for MR images, which are typically acquired in a 16-bit integer format. These normalization methods ensure, that intensity values are near $[-1, 1]$ or strictly between $[0, 1]$, before model training [14, 56]. While Minmax normalization shifts and scales the full intensity range of an image to a new given finite range, clipped Minmax (cMinmax) additionally clips at image percentiles, typically 1-5% at the intensity range borders, for better robustness. This comes with the drawback of information loss. Other variants of Minmax utilize quantiles for scaling without clipping, or estimated percentiles based on a region-of-interest (ROI) contained in the image. This typically requires a delineated ROI or at least a landmark. Common types of ROIs are the image foreground or a certain tissue type. For example, the WhiteStripe normalization [57] computes the mean μ_{WM} and the standard deviation σ_{WM} in a white matter region of the brain. Afterwards, these parameters are used to shift and scale the intensity values. Zscore normalization [55] normalizes the intensity value distribution to have a zero mean and a unit standard deviation. Therefore, each pixel value is subtracted by the image mean and then divided by the standard deviation. This normalization technique brings pixel intensities to a standardized scale, and hence, the relative importance of different features within an image becomes more consistent, facilitating effective comparison and downstream analysis. In contrast to Minmax or clipped Minmax, the output value ranges, i.e. the minimum and maximum values, are not fixed and may differ after Zscore normalization. Zscore normalization is also more robust against intensity outliers in an image. Quantile normalization [54], is similar to Zscore normalization, but utilizes the median $I_{50\%}$ instead of the mean, and the interquartile range (IQR) instead of the standard deviation. Typically, it is less biased by outliers in the image histogram. The resulting intensity value distribution has zero median and unit IQR. However, in case of a large fraction of (almost) equal intensity values, i.e. $\text{IQR} = I_{75\%} - I_{25\%} \approx 0$, e.g. due to a large fraction of homogeneous background, the scaling may become extensively large or even undefined. In addition, normalization methods have been developed specifically for MR (piece-wise linear histogram matching [58]) or even specifically for brain MR images (cf. WhiteStripe [57]) in order to obtain quantitative comparable intensities for the same brain or body structures. This results in an image where the local intensity value distribution of the white matter ROI

Table 1. Overview of normalization methods. The target intensity range $[j_1, j_2]$ can be chosen arbitrarily, but is typically set to $[0, 1]$ or $[-1, 1]$.

Method	Description	Result range	References
Minmax	Shifts and scales image intensity values to a range with given minimum and maximum value.	$[j_1, j_2]$	[54]
cMinmax	Clips at lower and upper percentiles before Minmax. More robust to high and low outliers.	$[j_1, j_2]$	
ZScore	Shifts the intensity values to a mean μ_I of 0 and scales to unit standard deviation σ_I .	$\mu_I = 0, \sigma_I = 1$	[54]
Quantile	Shifts the intensity values to a median of 0 and scales to a unit inter-quartile range ($IQR = I_{p75\%} - I_{p25\%}$).	median(I)=0, IQR=1	[54]
Binning	Binning: All intensity values are mapped to B ($=256$) equidistant bins.	$[0, B - 1]$	
PL	Piecewise-Linear: The histogram is scaled linearly in two pieces to match three landmarks of a standard histogram derived from a set of reference images.	depends on reference dataset	[58]

has zero mean and unit standard deviation. In a similar fashion, other normalization types besides Zscore can be adapted. For instance, for deep learning based MRI liver tumor segmentation [59], a Minmax normalization was applied by linearly mapping the 2% and 98% percentiles $I_{2\%}^{\text{Liver}}$ and $I_{98\%}^{\text{Liver}}$ of the local intensity distribution within a ROI in the liver, to 0 and 1. In order to match histogram modes and minimum and maximum percentiles of an MR dataset showing the same body region, a piece-wise linear standardization procedure[58] has been proposed. The authors argue that MR images exhibit an unimodal or bimodal histogram for most body regions, where the foreground concentrates around the first or second mode. In a first step, minimum and maximum percentiles, as well as the first or second (in case of a bimodal histogram) modes of images in a training or reference data set are obtained and normalized. In the second step, the intensity ranges below and above each mode are piece-wise linearly scaled to match the normalized modes and percentiles of the reference data set. This ensures, that the image histograms match at three important landmarks: The lower percentile, the (second) mode and the upper percentile. Binning can be regarded as a normalization method to convert float values to 8-bit integer values. In this case 256 bins are used. It also removes information, because close but different intensities are mapped to the same bin value. By additionally copying the binned gray value to three color channels, images can further be converted to RGB images. Binning is needed for some metrics, because they require a finite number of intensity values (see Sec.2.8), or it is used to easily apply a method for 8-bit images to a binned float valued image. The normalization methods investigated within this study are defined in detail in the supplement in Sec. A.2, an overview is shown in Tab.1.

2.3 Reference Metrics

Reference metrics are based on comparing a reference image R with another image I . Both images are assumed to have the same spatial dimensions. An overview of the reference metrics analyzed in this study is given in Tab.2. If the image I was not acquired with the same modality or the same time point as image R , spatial alignment has to be ensured before applying a reference metric. Typically, this is achieved by image registration techniques.

Slight spatial misalignment between paired images has been identified as a problem when evaluating with reference metrics, such that specialized methods have been investigated for this purpose. By assessing similarity in the complex-wavelet domain, complex-wavelet SSIM (CW-SSIM) is able to ignore small translations, scaling and rotations [68]. A score derived from features of the Segment Anything Model (SAM), mainly compares semantic features and therefore better ignores different style and small deformations [86]. The learned Deep Image Structure and Texture Similarity (DISTs) metric gives more weight to texture similarity, ignoring fine-grained misalignment of these textures [73].

For natural images, a large set of reference metrics has been benchmarked on the Tampere Image Dataset [27] or the LIVE Image Quality Assessment Database [29]. Many of the standard metrics from natural imaging have been frequently applied to medical images. However, some careful modifications are necessary for images with a data type other than 8-bit unsigned integer. In the following, we introduce the investigated reference metrics with some more detail and background and highlight important adaptions. A full list of metrics and their calculation is found in the supplement in Sec. A.3.

Table 2. Overview of similarity (reference) and quality (non-reference) metrics. [Implementation sources: gh=gitHub, itk=Insight Segmentation and Registration Toolkit[60], np=numpy[61], pypi=python package index, skl=scikit-learn[62], ski=scikit-image[63], tm=torchmetrics[64]]

Group	Abbre-viation	Description	Similarity ↑ [min, max]	Imple-mentation	Ref.
Similarity (Reference) Metrics	SSIM	Structural Similarity Index Measure: combination of structure, luminance and contrast	[0, 1] ↑	tm, ski	[65]
	MS-SSIM	Multi-Scale SSIM: SSIM on original and 4 downscaled image resolutions	[0, 1] ↑	tm	[66]
	CW-SSIM	Complex Wavelet SSIM: ignores phase shifts in the wavelet domain, ignores small rotations and spatial translations	[0, 1] ↑	gh [67]	[68]
	PSNR	Peak Signal-to-Noise-Ratio: relation of data range to MSE	[0, ∞] ↑	tm, ski	[69]
	NMSE	Normalized Mean Squared Error	[0, ∞] ↓		
	MSE	Mean Squared Error	[0, ∞] ↓	skl	
	MAE	Mean Absolute Error	[0, ∞] ↓	skl	
	LPIPS	Learned Perceptual Image Patch Similarity	[0, 1] ↓	pypi [70], tm	[71]
	DISTS	Deep Image Structure and Texture Similarity Metric	[0, 1] ↓	gh[72, 67]	[73]
	NMI	Normalized Mutual Information: MI with fixed range	[1, 2] ↑	ski	
Down-stream	PCC	Pearson Correlation Coefficient	[0, 1] ↑	skl	
	DICE	segmentation metric, evaluating overlap	[0, 1] ↑	itk	
Quality ↑					
Quality (Non-Reference) Metrics	Blurriness	BE	Blur Effect: difference of gradients when additionally blurred	↓	ski [23]
		BR	Blur Ratio: ratio of blurred pixels to edge pixels	↓	- [74]
		MB	Mean Blur: sum of inverse blurriness divided by number of blurred pixels	↑	- [74]
		VL	Variance of Laplacian	↓	ski+np [75]
		BEW	Blurred Edge Widths	↓	- [76]
		JNB	Just Noticeable Blur	↓	gh(C++)[77] [78]
		CPBD	Cumulative Probability of Blur Detection	↑	gh[79] [80]
	MR Quality	MLC	Mean Line Correlation (also average structural noise): mean correlation between neighbored rows and columns	↓	- [81]
		MSLC	Mean Shifted Line Correlation (also average nyquist ghosting): mean correlation between rows and columns, that are with half image distance apart	↓	- [81]
		BRISQUE	Blind/ Referenceless Image Spatial Quality Evaluator	↓	pypi[82] [83]
Noisi-ness	NIQE	Natural Image Quality Evaluator	↓	gh[84]	[85]
	MTV	Mean Total Variation: Mean L2-normed gradient in x- and y- direction	↓	-	[25]

2.4 Structural Similarity Index Measure

The structural similarity index measure (SSIM) combines image structure, luminance, and contrast, which are calculated locally for each pixel. By relating local covariance of image I and reference image R to the local standard deviation of both images, the structure component is assessed. Luminance relates both local mean values, while contrast is defined by both standard deviations. The local SSIM is calculated for each pixel within a small neighborhood and weighted with a Gaussian kernel. For the final SSIM, the local SSIM is then averaged over all pixel locations. The upper bound for the SSIM is 1, which is achieved when two identical images are given as input. The SSIM decreases with lower similarity down to 0, which constitutes its lower bound. Several variants of SSIM exist. Multi-scale SSIM (MS-SSIM) [66] calculates local luminance, contrast and structure additionally for four down-scaled versions of the images. These are then combined with empirically determined weights to a local MS-SSIM value, which is also averaged over all pixels for a final MS-SSIM score. MS-SSIM is more sensitive towards large-scale differences between the images to be compared. This puts less impact on high resolution details. The complex-wavelet SSIM (CW-SSIM) [68] was specifically designed to compensate for small rotations and spatial translations. For this metric, only the coefficients of the complex-wavelet transformed images I and R are used, such that small phase shifts between both images are ignored. This additional freedom may allow unnatural results, when CW-SSIM is used for model optimization [87]. As an adaption of SSIM to float valued images, the data range parameter L (see Sec. 2.1) is used to scale the internal constants $C_1 = (k_1 \cdot L)^2 = (0.01 \cdot L)^2$ and $C_2 = (k_2 \cdot L)^2 = (0.03 \cdot L)^2$ (and $C_3 = C_2/2$), which are used to make computations numerically stable (see supplement Sec. A.3, Eq. (41)). It can be derived from the SSIM calculation, that a high data range parameter L and thereby high values for $C_1 - C_3$, lead to SSIM values near 1, because the constants $C_1 - C_3$ dominate the calculation compared to the observed intensity values. In these cases, SSIM is not very informative. This has been experimentally observed before [51], and a default normalization of float value ranged images to the range $[0, 1]$ and a modification of constants $C_1 = C_2$ to $(k_1 \cdot L)^2 = (0.0001 \cdot 1)^2 = 1 \cdot 10^{-8}$ was proposed. Common implementations also define different default values for L . As the `skimage` [63] package generally assumes float valued images to be in the range $[-1.0, 1.0]$, its implementation of SSIM defines $L = 2$ as default. The `torchmetrics` [64] implementation of SSIM sets $L = L_{I,R}$ as default for images I and R . The choice for the data range parameter L is directly related to normalization techniques that rescale image intensities: If images I and R are scaled by factor a to $I' = I \cdot a$ and $R' = R \cdot a$, then calculating SSIM on I' and R' with $L' = L \cdot a$ will be the same as calculating SSIM on I and R with L . However, if image intensities are additionally shifted by an additive value b , the luminance term will increase with b and yield different SSIM values. If this shift b is negative, as it typically is with Zscore normalization (see supplement Sec. A.2, Eq. (3)), this can lead to negative SSIM values [50].

2.5 Peak Signal-to-Noise Ratio

Peak signal-to-noise ratio (PSNR) was developed to measure the reconstruction quality of a lossy compressed image compared to the uncompressed reference image [69]. However, it is frequently used as a metric for assessing image similarity. The PSNR is infinite for identical images and decreases monotonically as the differences between image I and reference R increase. The data range parameter L is incorporated in the PSNR as the peak signal. The noise in the PSNR is calculated as the mean squared error (MSE, see 2.6). The PSNR (see supplement Sec. A.3, Eq. (39)) is minimal, i.e. 0, when $L = \sqrt{\text{MSE}(I, R)}$, and for $L > \sqrt{\text{MSE}(I, R)}$, PSNR strictly increases with increasing parameter L . For natural images, improved variants of PSNR called PSNR-HVS and PSNR-HVS-M, that seem to correlate closer to the human visual system [27], have been developed. Adapted implementations for variable intensity ranges and experiments with medical images are not available at this time. A deeper exploration of these metrics remains important future work.

2.6 Error Metrics

This group of metrics, including mean absolute error (MAE), mean square error (MSE), root mean square error (RMSE) and normalized mean square error (NMSE), directly depends on the absolute difference of intensity values at equal pixel locations. The metrics MSE, RMSE, and NMSE are based on the squared difference and due to convex shape of the quadratic function, these metrics give more weight to large differences than MAE, which is based on the unsquared absolute difference. By normalization with the standard deviation of the reference image, NMSE assigns a higher similarity to images with a higher standard deviation, i.e. with high variation and a large range of intensity values. On the contrary, the same intensity differences lead to a lower similarity, if the reference image has a very low standard deviation, i.e. it appears very homogeneous. However, the scale and range of all these metrics strongly depend on the intensity value ranges and, thereby, also on the normalization method.

2.7 Learned Metrics: LPIPS and DISTS

Learned perceptual image patch similarity (LPIPS) relies on image feature maps from a trained image classification model. For the LPIPS metric, an Alex-Net or VGG-architecture trained for classification on ImageNet was employed and linear weights were optimized by jointly training a second network to predict human judgements on a dataset comprising these judgements for distorted image patch pairs named Berkeley-Adobe Perceptual Patch Similarity (BAPPS) Dataset [71]. The VGG version

of LPIPS was recommended for usage as a traditional perceptual loss, while the Alex-Net version should be preferred as a forward metric. The latter one is also faster at inference due to the smaller network, so we analyzed LPIPS with Alex-Net in Sec. 3. Even though the networks were trained on RGB images, the trained networks expect an input range of $[-1, 1]$, e.g. by previous Minmax normalization. LPIPS has shown great correlation with human perception and outperforms many other similarity metrics on natural images [71]. It has occasionally been used for validation of medical image synthesis [88], and is commonly applied as perceptual loss for training medical image-to-image translation models [3].

The Deep Image Structure and Texture Similarity (DISTS) metric is an adaption of LPIPS giving more focus on texture. The overall DISTS metric is obtained by averaging weighted combinations of structure and texture similarities across network layers at different depth levels. Compared to LPIPS, the max-pooling layers in the feature extraction network were replaced by ℓ_2 -pooling layers for better anti-aliasing [89], and the input image was added as a zeroth feature map on top of the convolved and downsampled feature maps from the feature extraction network. The Euclidean feature distance measurement is replaced by global SSIM feature distance measurement and weighting factors α for structure and β for texture features were optimized to achieve similar scores on different samples of equal textures from a texture dataset [73].

2.8 Statistical Dependency Metrics: NMI and PCC

Mutual information (MI) estimates the amount of information of an image R , that can be predicted from image I . MI is widely used as an optimization criterion for multi-modal image registration [90]. It has been used sporadically as a metric for validation of image synthesis [55, 44]. A high value of MI indicates that there is a significant amount of shared information between the two images, implying strong dependency or similarity. The upper bound is attained for $I = R$. The normalized mutual information (NMI) is an adaptation of the MI metric that accounts for the variations in the entropy of the images being compared. NMI is particularly useful in scenarios where images have different entropy levels, as it normalizes the MI value to provide a more standardized measure of similarity. NMI adjusts the raw MI by considering the joint entropy of the images. The NMI has a fixed value range of $[1, 2]$, which is preferable for comparing absolute metric scores and interpretability. A maximum similarity is achieved for $I = R$, resulting in a maximum NMI value of 2. The Pearson correlation coefficient (PCC), is a statistical dependency metric which measures the degree of linear dependency between the intensities in I and R at each pixel location. The value range of the PCC is $[-1.0, 1.0]$. In case of perfect (negative) linear correlation between I and R the PCC value is 1.0 (-1.0). The PCC may indicate very low similarity with values around 0.0, if the relation between pixel values in image I and R is non-linear or uncorrelated. As PCC is defined by correlation and NMI and MI both operate on normalized binned images, previous normalization that purely scales and shifts, such as Minmax, Zscore or Quantile normalization, does not have any effect on the resulting scores.

2.9 Indirect Evaluation with Downstream Tasks

Another option for validation is to consider which tasks are going to be performed downstream from a synthesized image. Whenever one of these tasks is performed, the quality of synthetic images can also be assessed by measuring the performance of the specific task on the image compared to the performance of the reference image. In medical image-to-image translation, which aims for improved medical diagnosis or treatment, assessing the performance of medical diagnosis or treatment directly derived from digital images is very desirable. In this context, synthetic images must be processed in the same way as the reference image and should have equal outcomes in the downstream task. However, deviations between synthetic images and reference images can be accepted, when they have no impact on the downstream task. As an example, if a synthetic MR image is generated for detecting a brain tumor, it is to some extent irrelevant if healthy brain tissue in the synthetic image is brighter or slightly differently structured than in the true reference image, as long as it is clearly identified as healthy tissue. If a synthetic histology image is rated with the same grade of cancer as the reference image, the exact cell-wise correspondence might not be important. Many downstream tasks on medical images can be nowadays performed automatically, including:

- Detection or segmentation of organs, cells and lesions, e.g. the Segmentation of brain tumors from T1-weighted native, T1-weighted contrast enhanced, T2-weighted, and fluid attenuation inversion recovery (FLAIR) MR images [42] [Related downstream task metrics: DICE, Intersection over Union (IoU)].
- Classification of images or image segments, e.g. the synthesis of clinical skin images with 26 types of conditions, verified by classification scores of dermatologists [91] [Related downstream task metrics: Accuracy, Precision, Recall, F1-Score].
- Transfer learning and data augmentation, e.g. the synthesis of chest X-ray for data augmentation and evaluation of classification model on real data with and without synthetic training data [92] [Related downstream task metrics: e.g. Sensitivity, Specificity, Area Under the Receiver-Operator-Characteristic curve (AUROC)].
- Multi-modal registration, e.g. the registration of synthesized MR image from CT image to MRI atlas instead of registration of CT image to MRI atlas [93] [Related downstream task metrics: MSE, MI].

- Dose calculation in radiation therapy planning, e.g. the synthesis of a planning CT from MRI for use in a radiation planning tool [94] [Related downstream task metrics: relative difference of planned radiation dose].

Detection, segmentation and classification metrics for the biomedical domain have been well documented and discussed [40, 41]. Therefore, the performance of such tasks with synthetic images can be well compared to the performance with reference images to validate the use of synthetic images for a specific task. The concept of downstream task evaluation metrics recognizes that the final goal of image synthesis in the medical domain is to generate useful and correct images rather than images, that are visually appealing [95]. However, if image synthesis was optimized regarding a certain downstream task, the resulting images might not be optimal for other non-related tasks. Specifically, they might have a fake appearance, that does not interfere with the downstream task, but would be misleading for direct review of medical practitioners. Furthermore, the evaluation of downstream tasks can substantially depend on the performance of the downstream task method. If a segmentation model fails on a large set of reference images, the comparison to segmentations on synthetic images is obsolete. The amount and variety of downstream tasks and corresponding metrics are almost unlimited, but to discuss and analyze the value of downstream tasks, we include the evaluation of a downstream segmentation model with a popular segmentation metric, namely the DICE score [96, 40].

2.10 Non-Reference Quality Metrics

Non-reference metrics, often also called quality metrics or blind metrics, try to assess the quality of a distorted image without knowing the undistorted reference. As a reference might not be available, these metrics can be applied in many evaluation settings. However, there is a huge amount of such metrics and most of them assume a certain kind of distortion to be detected. The correlation of many of these metrics with human perception has been investigated [26]. But also deviations between these scores and diagnostic quality perceived by radiologists have been observed [97]. Blurriness metrics were quite successful in detecting images with reduced quality as perceived by humans in different image domains.

In this paper, we select and present a set of quality metrics (see Tab. 2) that could complement reference metrics and detect especially those distortions, which reference metrics can miss. It has often been discussed [98, 5], that error metrics are not sensitive to blurring, which can be problematic because synthesis models may create blurry results. That is why we evaluated a set of blurriness metrics, that do not need a reference. Similar to the learned similarity metrics, also learned quality metrics have shown to provide useful quality scores for natural images [83, 85]. Last, we assessed metrics, that detect MR acquisition artifacts [81] or noise [25].

2.10.1 Blurriness Metrics

A large set of metrics has been developed to measure the sharpness or, inversely, the blurriness of images to filter out low-quality images. Methods assessing image blur operate either on the spatial domain, the spectral domain, e.g. through wavelet or fast Fourier transform. In addition, there are learned blur detection methods as well as combinations [99]. Blur assessment methods in the spatial domain can exploit local image gradients. Others rely on binary edge detection, with the drawback, that thresholds are needed to decide which pixel belongs to an edge and which one does not. Hence, thresholds need to be adapted for varying intensity value ranges. In general, spectral domain transforms are computationally more costly, so methods on the spatial domain tend to perform faster.

The Blur-Effect [23] metric estimates the strength of blur by additionally blurring the image and assessing how much the sum of all local gradients has decreased. For originally sharp images, the additional blurring strongly decreases intensity changes. For already blurred images, additional blurring has less effect on the image gradients.

The Laplacian operator allows to compute an approximation of the image gradient, which indicates sharp edges by locally high gradient values. The variance of the Laplacian (VL) therefore accounts for many sharp edges and decreases for blurred images. It has been used for auto-focusing of microscopic viewing planes [75].

The mean blur (MB) and blur ratio (BR) metrics were jointly [74] designed to assess blurriness and edges. Every pixel's intensity is related to the average of its neighbor's intensities. This ratio is called inverse blurriness. In a second step, edge pixels are identified by comparing the local gradient value to the mean of all gradient values of the image and by selecting only those pixels as edge pixels, that are placed on local maximum gradients. For the BR metric, edge pixels exhibiting inverse blurriness below a threshold of 0.1 are counted as blurred pixels. The BR metric is then defined as the ratio of counted blurred pixels to edge pixels, while the MB metric is defined as the summarized inverse blurriness divided by the number of blurred pixels. In summary, the BR metric increases with the number of detected blurred pixels and decreases with the number of detected edge pixels. The MB metric is based on inverse blurriness and therefore decreases with blurriness. When the number of blurred pixels increases, this further reduces the MB metric.

A set of blurriness metrics has been derived from the concept of measuring the width of an edge [76]. First, edge and non-edge pixels are detected, e.g. with the canny algorithm [100]. Second, edge pixels are traced along their detected dimension to find the next pixel with a differently signed gradient, which marks the end of the edge. The distances of all edge pixels to the ends

of their respective edges are summed as the blurred edge widths (BEW) metric, which means that higher values indicate wider and thereby more blurry edges. This idea was extended with a notion of just noticeable blur (JNB) [78], which evaluates the image in smaller blocks. Only blocks with a sufficient fraction of edge pixels are considered. The edge widths are additionally weighted with the just noticeable blur width, which was assessed experimentally as the edge width, that is noticeable as blur, given a local intensity contrast.

A further blurriness metric measures the cumulative probability of blur detection (CPBD) [80] extending the approach of JNB. The edge widths are similarly weighted by the just noticeable blur width and then the probability of detecting blur in a pixel of an edge block is modelled as an exponential function. Then the CPBD metric corresponds to the cumulative probability of not detecting blur in any of the preprocessed edge pixels. The incorporated just noticeable blur width is based on experiments with 8-bit integer valued images. Therefore, image intensity values should be binned to the range [0, 255] in order to reasonably apply JNB or CPBD.

As a popular edge detection algorithm, canny edge detection [100] can be used for BEW, but a lower and higher threshold for detecting edge pixels from the image gradient must be configured. To adapt to different value ranges the thresholds can be chosen relatively to the data range L . In our experiments, we use 10% and 20% of L as the lower and higher thresholds for edge detection in BEW, JNB and CPBD.

2.10.2 MR Quality Metrics

In MR images, specific artifacts may appear, which are related to image acquisition and reconstruction. These artifacts may not only appear on real images, but could be reproduced in synthetic images, which is undesirable. Therefore, the use of MR specific quality metrics could efficiently improve validation of MR synthesis models. In order to select the preferred image from a repeated set of image acquisitions of the same patient, Schuppert et al. [81], evaluated a set of image quality metrics. Mean line correlation (MLC, in [81] denoted as "average structural noise") and mean shifted line correlation (MSLC, in [81] denoted as "average nyquist ghosting") were revealed to be among the best metrics to predict which image was preferred among repeated acquisitions. Possibly, these metrics are able to detect common MR acquisition artifacts, such as ghosting or motion artifacts, that would lead to repeated acquisitions. The MLC metric is defined as the mean correlation between neighboring lines of pixels in an image. The MSLC metric is defined as the mean correlation between image lines, that are separated by half of the image width or height respectively.

2.10.3 Learned Quality Metrics

Similar to learned reference metrics, also non-reference metrics have been developed from learned image features. The blind/reference-less image spatial quality evaluator BRISQUE [83] leverages 18 spatial image features extracted from distorted training images of the LIVE database [29] annotated with a quality score. A simple support vector machine regression model was trained to predict the annotated quality scores from the extracted set of features.

The natural image quality evaluator (NIQE)[85] does not rely on training with annotated images. Instead, a multi-variate Gaussian model is parameterized from the same set of 18 spatial features, but extracted from two scales. A reference model was parameterized from features from a training set of undistorted images to obtain the multivariate Gaussian model. Images were selected from copyright free Flickr data and from the Berkeley image segmentation database [101]. The NIQE metric assesses the distance of fitted test image parameters to the parameters of the reference model. Due to the characteristics of the training set and assumed differences to MR images regarding intensity value distributions, the NIQE metric may not be directly transferable to MR images.

2.10.4 Noise Metrics

For denoising of images, total variation [25] has been used as a criterion for noisiness. Therefore, mean total variation seems promising as a measure of undesired noise. It is defined by the local differences between neighbored pixels.

Because noise can be reduced by blurring, blurriness metrics might act as inverse noisiness metrics. In other words, an increasing degree of blurriness may correlate with decreasing noise. Inversely, adding noise may disguise blurriness and therefore impair blurriness metrics for image quality assessment.

3 Experiments

In order to systematically investigate reference and non-reference metrics, we distorted 100 T1-weighted contrast enhanced MR images with 11 different types of distortions in five strengths. For the reference metrics (see Sec. 2.3), the similarity between each distorted image and its undistorted reference was calculated. For the non-reference metrics (see Sec. 2.10), the metric scores for all distorted and undistorted images were assessed. For the segmentation metric (see Sec. 2.9), we trained a model and predicted segmentations for all distorted and undistorted images. The segmentation metric assessed the agreement between segmentations derived from distorted images and segmentations derived from the respective undistorted reference image. In addition, images were left with raw intensity values or individually normalized with one of five different normalization methods.

In image-to-image tasks, MR source or target images are typically normalized for model training and the synthesized images are generated in this normalized space. Validation of synthesized images can either be performed in this normalized space, such that the normalized target image is used as reference and the synthesized image is assumed to already be normalized appropriately. Another possibility is to invert the previously performed normalization method on the synthesized image to the original intensity range. Then the synthesized image can be compared to the target image in the original intensity range. In our experiments, we test the metrics in the original and a normalized intensity range. As some distortions slightly or more drastically extend or reduce the intensity range of the reference image, different normalization methods result in different alignment of histograms of the reference and the distorted images. Examples of differently normalized reference and distorted images and their histograms are shown in the supplemental Figs. S.1 and S.2.

The LPIPS metric requires an input range of [-1 and 1], therefore we decided to apply Minmax and cMinmax normalization to the required target range of [-1, 1]. The DISTS metric requires an input range of [0, 1].. Even though all normalization methods besides Minmax and cMinmax do not satisfy the required input ranges, we did evaluate the metrics after these metrics to investigate deviations to the recommended type of normalization.

3.1 Data

The data was taken from the BraSyn 2023 challenge [102] training set, which consists of 1251 T1-weighted (T1n), T1-weighted contrast-enhanced (T1c), T2-weighted (T2w), T2-weighted FLAIR (T2f) and tumor segmentation masks of three classes (whole tumor, tumor core, enhancing tumor). We selected the first 100 cases of the T1c training set images as reference images. For better visualization and reduced computation time, we extracted the centered 2D slice of each 3D volume.

3.2 Segmentation model for downstream task

We trained an automatically configuring U-Net based segmentation network [103] on the T1c images of the BraSyn dataset to perform a segmentation task with three classes (1: whole tumor, 2: tumor core, 3: enhancing tumor). The architecture of the U-Net included five residual blocks, with downsampling factors 1, 2, 2, 4 and 4, initially 32 features and one output channel activated by a sigmoid function per class. Although the segmentation masks of the BraSyn data originally consist of 4 classes (3 tumor classes and background), the model was trained with 3 output channels, assuming that a class was present, when the respective output channel exceeded a threshold of 0.5, and when all higher indexed classes were not preset. As a preprocessing step for training and inference, Zscore normalization was applied to the input images. Therefore, no other normalization methods were tested. The segmentations were evaluated with the DICE score (see supplement Sec. A.3, Eq. (18)) for the foreground (combination of all tumor classes) and for each class individually.

3.3 Distortions

We selected a wide range of distortions, which we expect to appear with MR image synthesis. The parameters of all distortions were scaled to five increasing strengths, where a strength of one should be a minimal distortion, which is not immediately visible and five a strongly visible distortion, which clearly impedes any diagnosis. We initially scaled the distortion parameters to comparable strengths by a reader study with six experienced researchers. The final parameters for each distortion are listed in the supplement in Sec. A.4. Examples for minimum (strength = 1) and maximum (strength = 5) distortions are shown in Tab. 3. Among the selected distortions, translation and elastic deformation were applied as spatial transforms, that are commonly found, when the reference is not well aligned to the image to be tested. This is frequently the case in image-to-image translation, when the input image was acquired with a different modality or at a different time point. Usually, the patient has moved in between and registration was possibly not sufficient. Translation was modeled as an equal shift of all pixels along the x and y-axis and parameterized with a fraction of the image width and height. Elastic deformation was modeled by placing a grid with a given number of points on the image, randomly displacing grid points, and linearly interpolating between the new point positions. The displacements were sampled from a normal distribution with increasing parameter σ and the number of points was reduced for higher distortion strengths. Intensity distortions, that shift, stretch or compress the histogram, such as gamma transforms or an intensity shift, can appear between different scanning parameters, because MR does not guarantee a fixed intensity scale. For gamma transforms, images are first normalized by Minmax to range [0, 1]. This ensures, that the intensity value range is unchanged under gamma transformation, which is simply potentiating with a parameter γ . Then, the intensities are scaled back to the original intensity range. We call gamma transforms for $\gamma > 1$ denominated "Gamma High", while those with $\gamma < 1$ are named "Gamma Low". Both types of distortions are parameterized with increasing or decreasing values of γ respectively for increasing distortion strengths. Intensity shifts are modeled by adding a fraction of the maximum intensity range to the intensity value of all pixels. Further distortions, that represent typical acquisition artifacts of MR images are ghosting, stripe and bias field artifacts. Ghosting artifacts appear as shifted copies of the image, arising from erroneous sampling in the frequency space. Scaling a single pixel with an intensity parameter in the frequency space causes artificial stripes. Bias fields appear as low frequency background signals, that we model by multiplying with an exponential of a polynomial function of degree three (see supplement Sec. A.3 Eq.(45)). All of these MR acquisition distortions may moderately expand the intensity range of the

distorted image compared to the reference image. Gaussian noise or Gaussian blurring are not restricted to MR acquisition but, as in most imaging modalities, they are frequently observed and were also analyzed in our study. Gaussian noise adds intensity values randomly sampled from a normal distribution with $\mu = 0$ and increasing σ to each pixel intensity. Gaussian blur convolves the reference image with a Gaussian filter with increasing σ . Last, we investigate the effect of replace artifacts, where parts of the image content are replaced, in this case by mirrored regions. In the BraSyn data set, in most cases, there is a tumor in exactly one hemisphere of the brain. By mirroring one hemisphere onto the other one, a second tumor is inserted into, or a tumor is removed from the second hemisphere. We scaled this distortion by mirroring an increasing fraction of the hemisphere. Replacing brain structures in one hemisphere by structure in the other one, simulates the generation of synthetic structures, that were not in the input image. This is a known problem of some synthesis models, e.g. of cycleGAN architectures [104]. The detection of such synthetically inserted structures is highly desired for image-to-image translation model validation.

Table 3. Examples of distorted images for lowest strength $s = 1$, where the difference is hardly visible, up to the maximal distortion strength $s = 5$. All distorted images are displayed with the same intensity range as the reference image, i.e. the range was clipped in case of higher or lower values.

Distortion	example images				Distortion	example images			
	$s = 1$		$s = 5$			$s = 1$		$s = 5$	
Intensity	Shift	Gamma	High	Gamma	MR Acquisition Artifacts	Shift	Gamma	High	Gamma
	Intensity	Low	High	Low		Intensity	Low	High	Low
	Trans-	Shift	Gamma	High		Intensity	Low	High	Low
	lation	Intensity	Low	High		Shift	Gamma	High	Gamma
	Elastic	Shift	Gamma	High		Intensity	Low	High	Low
	Deform	Intensity	Low	High		Shift	Gamma	High	Gamma
						Intensity	Low	High	Low
						Shift	Gamma	High	Gamma
Other Distortions					Replace	Gaussian	Gaussian	Blur	Blur
					Artifact	Noise	Blur	Blur	Blur

4 Results

4.1 Reference Metrics

The complete results for all reference metrics, all distortion strengths and all normalization methods are contained in the Supplementary Figs. S.3-S.5. There, for each metric and normalization method, the trends of all distortions for increasing strengths are shown. The selected and compressed results in Tab. 4, contain the median metric values over all strengths and images for one selected and recommended normalization method. For LPIPS and DISTs, images were normalized by Minmax to range $[-1, 1]$ and $[0, 1]$, for DICE, the images were Zscore normalized, and for all other metrics, we did not apply normalization. Tab. 4 only contains the DICE score on the foreground (union of all three tumor classes), as the DICE segmentation scores for all three classes are very similar (see Supplementary Fig. S.10). The results are described in the following, ordered by distortions.

Bias Field has a moderate effect to most metrics. MS-SSIM is much more sensitive to simulated bias field artifacts than simple SSIM or CW-SSIM. The error metrics show clearly increased (dissimilarity) scores, while the LPIPS score is hardly effected. Compared to other distortions, PCC drops noticeably with bias field distortions. **Ghosting** generally has a weak effect on most

Table 4. Median metric values for each distortion evaluated on 100 images and all distortions strength. All metrics scores shown here were assessed on images without normalization, except LPIPS*, DISTS* and DICE*. The darker the background the higher the sensitivity of the metric to the respective distortion compared to all other distortions. The arrows indicate, if the metric increases (\uparrow) or decreases (\downarrow) with higher similarity. *: For LPIPS Minmax normalization to [-1, 1] was used, for DISTS Minmax normalization to [0, 1] was applied and DICE scores were assessed after Zscore normalization and segmentation.

metrics	SSIM \uparrow	MS- SSIM \uparrow	CW- SSIM \uparrow	PSNR \uparrow	MAE \downarrow	MSE \downarrow	NMSE \downarrow	LPIPS* \downarrow	DISTS* \downarrow	NMI \uparrow	PCC \uparrow	DICE* \uparrow
Distortions												
Bias Field	0.96	0.89	0.92	28.05	204.43	2.00·10 ⁵	324.16	0.06	0.08	1.32	0.91	0.92
Ghosting	0.93	0.99	0.98	42.23	34.58	3.58·10 ³	3.52	0.02	0.11	1.46	1.00	0.97
Stripe Artifact	0.52	0.98	0.99	33.72	94.77	2.07·10 ⁴	22.17	0.11	0.33	1.37	0.99	0.90
Gaussian Blur	0.98	1.00	1.00	38.27	21.11	4.65·10 ³	5.17	0.07	0.12	1.52	1.00	0.93
Gaussian Noise	0.58	0.92	0.98	31.54	181.33	5.16·10 ⁴	47.68	0.44	0.32	1.21	0.97	0.86
Replace Artifact	0.95	0.94	0.92	30.80	35.35	5.10·10 ⁴	47.77	0.04	0.05	1.64	0.98	0.71
Gamma High	0.89	0.84	0.80	22.19	315.44	3.31·10 ⁵	299.66	0.08	0.14	1.79	0.98	0.90
Gamma Low	0.96	0.94	0.92	21.07	312.06	3.26·10 ⁵	273.75	0.04	0.09	1.81	0.99	0.89
Shift Intensity	0.29	0.99	0.91	17.69	1.17·10 ³	1.37·10 ⁶	1.20·10 ³	0.00	-0.00	2.00	1.00	1.00
Translation	0.72	0.52	0.65	21.24	306.77	5.61·10 ⁵	509.30	0.24	0.08	1.13	0.72	0.29
Elastic Deform	0.92	0.96	0.96	30.91	56.64	4.42·10 ⁴	41.92	0.04	0.08	1.39	0.97	0.92

Table 5. Comparison of **relative** metric scores for selected distortions for comparison of normalization methods. As a relative metric score, the median of one selected distortion is divided by the median metric score of all distortions. The gray background indicates higher sensitivity in the comparison of two normalization methods. LPIPS, DISTS and DICE metric are not shown, due to fixed recommendations regarding the normalization method.

metrics	Norm.	SSIM \uparrow	MS- SSIM \uparrow	CW- SSIM \uparrow	PSNR \uparrow	MSE \downarrow	NMSE \downarrow	MAE \downarrow	NMI \uparrow	PCC \uparrow
Distortions										
Gamma High	Standard	0.98	0.87	0.83	0.75	3.08	5.77	4.52	1.22	0.99
	cMinmax _{5%}	1.07	1.02	0.99	1.00	1.17	0.98	0.96	1.31	1.00
Gamma Low	Standard	1.05	0.97	0.95	0.71	3.05	5.69	4.13	1.23	1.01
	cMinmax _{5%}	1.07	1.02	1.00	1.13	0.77	0.48	0.47	1.31	1.01
Gaussian Noise	Standard	0.64	0.96	1.02	1.06	1.77	0.90	0.72	0.82	0.98
	Minmax	0.26	0.95	0.95	0.71	4.81	6.38	6.90	0.82	0.98
Ghosting	Standard	1.03	1.03	1.02	1.42	0.34	0.06	0.05	0.99	1.01
	Minmax	0.39	1.02	1.00	0.95	2.32	1.37	1.42	0.99	1.01
Stripe Artifact	Standard	0.57	1.02	1.03	1.14	0.93	0.36	0.33	0.93	1.00
	ZScore	0.84	1.01	1.02	0.98	1.78	0.95	0.95	0.93	1.00

Table 6. Comparison of metric scores for different distortion strengths of Translation and Elastic Deform. All metrics scores shown here were assessed on images without normalization, except LPIPS*, DISTS* and DICE*. *: For LPIPS Minmax normalization to [-1, 1] was used, for DISTS Minmax normalization to [0, 1] was applied and DICE scores were assessed after Zscore normalization and segmentation.

metrics	s	SSIM \uparrow	MS- SSIM \uparrow	CW- SSIM \uparrow	PSNR \uparrow	MSE \downarrow	NMSE \downarrow	MAE \downarrow	LPIPS* \downarrow	DISTS* \downarrow	NMI \uparrow	PCC \uparrow	DICE* \uparrow
Distortions													
Reference	0	1.00	1.00	1.00	8	0.00	0.00	0.00	0.00	0.00	2.00	1.00	1.00
Translation	1	0.83	0.87	0.98	26.39	143.10	2.13·10 ⁵	186.02	0.07	0.08	1.27	0.92	0.83
Elastic Deform	5	0.88	0.92	0.91	28.24	105.88	1.30·10 ⁵	116.73	0.06	0.11	1.32	0.95	0.86

Table 7. Median non-reference quality metric values for each distortion over 100 images. All metrics were assessed with binning normalization. The darker the background the higher the difference to the median metric value of the reference images. The arrows indicate, if the metric increases (\uparrow) or decreases (\downarrow) with image quality.

metrics	$BF\uparrow$	$BR\uparrow$	$MB\uparrow$	$VL\downarrow$	$MTV\downarrow$	$BEW\uparrow$	$JNB\uparrow$	$CPBD\downarrow$	$BRISQUE\downarrow$	$NIQE\downarrow$	$MSLC\downarrow$	$MLC\downarrow$
Distortions												
Bias Field	0.34	2.20	4.55	$5.71 \cdot 10^5$	127.29	3.26	15.96	0.61	69.46	23.10	0.16	0.97
Ghosting	0.33	5.89	0.93	$2.95 \cdot 10^5$	104.25	3.50	24.89	0.58	53.81	22.56	0.19	0.84
Stripe Artifact	0.24	0.07	$3.59 \cdot 10^3$	$1.20 \cdot 10^6$	327.94	2.66	6.72	0.89	155.84	93.27	0.28	0.38
Gaussian Blur	0.41	2.37	5.39	$2.75 \cdot 10^4$	68.80	5.42	70.00	0.28	73.69	24.97	0.19	0.98
Gaussian Noise	0.21	0.40	5.92	$1.51 \cdot 10^6$	459.26	3.13	11.57	0.75	43.70	37.06	0.15	0.56
Replace Artifact	0.33	1.92	5.44	$3.33 \cdot 10^5$	104.79	3.36	22.51	0.59	63.42	23.20	0.17	0.97
Gamma High	0.30	1.76	5.13	$1.51 \cdot 10^5$	57.30	3.24	13.80	0.62	69.61	23.59	0.15	0.95
Gamma Low	0.34	1.59	114.79	$5.62 \cdot 10^5$	127.82	3.46	25.43	0.57	62.69	22.86	0.18	0.97
Shift Intensity	0.33	1.93	5.32	$3.44 \cdot 10^5$	105.77	3.41	22.75	0.59	62.91	23.56	0.17	0.97
Translation	0.36	2.14	4.62	$1.27 \cdot 10^5$	90.11	4.17	35.52	0.48	63.72	21.91	0.17	0.98
Elastic Deform	0.36	2.13	4.64	$1.55 \cdot 10^5$	90.27	4.24	36.28	0.48	62.99	23.05	0.18	0.97

metrics, except on NMI and DISTs. **Stripe Artifacts** strongly influence a subset of metrics, including SSIM, LPIPS, DISTs and NMI, while most other metrics are not sensitive to this type of distortion. **Blurring** is hardly accounted for by most metrics, the strongest changes can be observed by the DISTs and NMI metrics. Regarding **Gaussian Noise**, SSIM is very sensitive, while MS-SSIM and CW-SSIM are not. The effect on error metrics is limited, while both learned metrics and NMI clearly indicate dissimilarity. **Replace Artifacts** are hardly detected by most metrics. Besides the DICE score, that aligns well with the distortion strength, PSNR and NMI are most sensitive. **Gamma transforms** with an increasing $\gamma > 1$ (Gamma High) or a decreasing $\gamma < 1$ (Gamma Low) similarly influence all metrics. All of them, except PSNR, assess the distortions with $\gamma > 1$ as stronger. Regarding constant **Intensity Shifts**, NMI and PCC are invariant. Their scores reflect perfect similarity. The same holds, when the images are normalized by any of the five normalization methods (see Supplementary Sec. B). Particularly for LPIPS and DISTs, Minmax normalization is recommended as standard. For all other metrics, except MS-SSIM and CW-SSIM, intensity shifts substantially decrease similarity. **Translation** strongly reduces the assessed similarity for all metrics besides DISTs. Even very small translations of strength $s = 1$, which corresponds to a 1% shift (2.4 pixels in our experiments), are clearly noticeable, as shown in Tab. 6. Only CW-SSIM is quite insensitive with respect to small translations, but is still very sensitive, when translation is strong. Compared to translation, **Elastic Deforms** only influence similarity metrics decently. Even stronger deformations have less impact on the metric scores, than the weakest translation does.

There are some coherent observations regarding the **normalization** method and certain types of distortions. Selected results are shown in Tab. 5. cMinmax_{5%} normalization reduces gamma transforms, such that most metrics are less sensitive to gamma transforms after cMinmax_{5%} normalization, compared to their standard normalization method. Minmax normalization amplifies Gaussian noise, Zscore normalization amplifies stripe artifacts.

Gaussian noise and stripe artifacts most strongly decrease the DICE score. Translated segmentations have decreasing overlap and thereby very low DICE scores. Tumors, which were inserted or removed by the Replace Reflect distortion are well indicated by decreasing DICE scores.

4.2 Non-Reference Metrics

The results for all non-reference metrics, all distortion strengths and all normalization methods are given in Supplementary Figs. S.6-S.9. The median metric scores are summarized in Tab. 7 for images, that were normalized by Binning, as most of the metrics were designed for 8-bit images. We describe the results ordered by quality metric groups.

All **Blurriness and Noisiness Metrics**, except MB, can distinguish well between different strengths of blurring. At the same time, the blurriness scores diverge in the opposite direction for increasing strengths of stripe artifacts and Gaussian noise. Only BEW scores are not influenced much by these distortions. All blurriness and noisiness metrics show coherent deviations for images with spatial Translation (see also Supplementary Figs. S.6-S.9). **MR Quality Metrics**, i.e. MLC and MSLC, clearly identify stripe artifacts. MLC is very sensitive to noise, but generally hardly reflects the distortion level. MSLC can identify ghosting, best with cMinmax_{5%} normalization (see also Supplementary Fig. S.8). The **Learned Quality Metrics** BRISQUE and NIQE clearly attest low quality to images with stripe artifacts. However, the BRISQUE score indicates higher quality for very weak stripe artifacts and for images with Gaussian noise or ghosting (see also Supplementary Fig. S.9). The NIQE score

indicates lower quality for Gaussian noise.

As BR, MB and NIQE were designed for and trained with 8-bit integer images, Binning normalization should be applied. The results for other normalization methods for these metrics are substantially different.

5 Discussion

The experiments demonstrate specific weaknesses of the popular SSIM and PSNR metrics. They are strongly decreased by constant intensity shifts if no normalization is applied. PSNR is very dependent on the kind of normalization, which complicates its use as a comprehensive metric for comparing studies of different authors. This has been pointed out before[55], but the normalization parameters are still not reported in many papers about medical synthesis models [50]. SSIM and PSNR underestimate blurring and thereby favor blurred images over differently distorted images. This is inline with reported findings of previous studies [105, 49]. SSIM and PSNR are both very sensitive to spatial translation, which is a frequently occurring issue in image-to-image translation, when paired input and target images are not acquired by the same hardware or not immediately at the same time points. The proper use of the data range parameter of SSIM for medical images and potential biases have been investigated [50], suggesting to use the dataset minimum and maximum values. In existing implementations of SSIM or PSNR, the default data range parameter might not be appropriate. For SSIM, although commonly applied on Zscore normalized MR images, a bias was demonstrated[50] with negative values, which we did not specifically investigate. Even though the generation of synthetic structures is an issue in image-to-image translation [104], highly relevant replace artifacts are not sufficiently assessed by SSIM and PSNR. Unexpected behaviour of SSIM and PSNR as mentioned above was illustrated by examples [106].

So how can these weaknesses be overcome? CW-SSIM is able to ignore small translations, due to calculation in the complex-wavelet domain. The DISTs metric also successfully focuses more on texture than spatial alignment. Precise registration would also strongly improve similarity assessment. However, interpolation may introduce blurring as shown by coherent variations of assessed quality by all non-reference quality metrics on spatially translated images. Our experiments also suggest, that a few strong local elastic deformations have a lot less impact on similarity metrics than rigid translations. At the same time, rigid registration is easier to solve via optimization than elastic registration, because only a few parameters need to be determined. Replace artifacts remain underestimated by most similarity metrics. For those artifacts, that resemble structures of diagnostic interest, the evaluation of segmentations with a specific segmentation model is useful. In our evaluation, we use a segmentation model, that was trained to detect different tumor regions. It successfully detects replace artifacts, where the tumor is doubled or removed.

The non-reference quality metrics can give valuable additional information about the quality of synthesized images. Blurring is easily and reliably detected by all blurriness metrics. However, MB and BR are not robust considering normalization, and display varying value ranges. For most metrics, assessed blurriness also decreases with other distortions, such as Gaussian noise, ghosting or gamma transforms, when these increase image contrast. Stripe artifacts shift image mean values and therefore Zscore normalization creates shifts between originally corresponding intensity values.

For assessing ghosting, the MR quality metrics MLC and MSLC were evaluated. The MLC metric represents the line-wise correlation between neighboring lines. The reference value in our experiments lies at 96%, which is probably caused by high anatomical consistency in the present pixel spacing. It strongly decreases for stripe artifacts, which fits to the fact, that the stripes change relations between local image intensities and are not oriented along the x- or y-axis. Random Gaussian noise reduces statistical correlation and thereby also MLC. Ghosting also reduces MLC, as it additionally distorts image intensities locally. The MSLC metric only slightly increases with ghosting, a bit more using cMinmax normalization. One reason could be the relative weak scaling of the ghost intensity in our experiments. In contrast, stripe artifacts significantly increased the MSLC metrics. Compared to MLC, by coincidence, stripes seem to be in the same phase at the half-image width distance and thereby drastically increase line-wise correlation.

Normalization methods can amplify or diminish distortions. Shift intensity is fully removed by all tested normalization methods. Gamma transforms are alleviated by cMinmax, because intensity values are compressed at very high and low intensity values. Gaussian noise and Ghosting, which extend the intensity value range compared to the reference image, are amplified by Minmax normalization, because the extended range is compressed and similar tissue types are no longer mapped to similar intensity values. Normalization methods can be viewed as methods to remove (intensity) distortions. Further distortions could be reduced by other methods, e.g. Bias field correction [107], which was designed to remove bias field artifacts.

Our experiments were performed on T1-weighted contrast-enhanced MR images of the human brain and are therefore restricted to the BraSyn dataset. Future work should include a much broader set of MR images with other sequences and body regions to make sure, that the results are valid more generally. The background in the BraSyn dataset takes up a large fraction of the image and was specifically preprocessed and set to 0. These factors largely influence some of the metrics, especially SSIM, PSNR and the error based metrics and therefore other data could yield different experimental results. We expect that using masks with these metrics will change absolute metric scores, but relative observations probably persist. However, the application of masks

with metrics, that do not assess similarity or quality on a per-pixel basis, but require a neighborhood, is still to be implemented as future work.

In comparison to other metric benchmarks, we do not compare the metric scores to human quality assessment. For each type of distortion, we tried to select five comparable strengths. As shown in Tabs. 3, the lowest and highest strengths were scaled to appear almost not visible or to decrease quality to an equally poor level. Even though distortion parameters might not be scaled perfectly to human perception, we assume, that the overall qualitative observations about which metrics are most sensitive towards which kind of distortions and the following conclusions are still valid.

6 Conclusions

For the validation of medical image-to-image translation, we gave a broad overview of possible metrics. For 11 reference, three non-reference metrics and a segmentation metric, we presented a detailed study of their sensitivity to 11 types of distortions, which are specific for MR images. As a conclusion, we give a few recommendations for the selection and application of appropriate validation metrics.

- As reference metrics, the combination of SSIM, LPIPS, MSE and NMI is able to detect a large set of undesired distortions. MS-SSIM, PCC, DISTS, NMSE, and MAE do not give much additional information. MSE is the most frequently used error metric and therefore best suited for comparison to previous studies. In general, the use of PSNR should not be recommended. CW-SSIM is appropriate in addition to ignore slight misalignments to reference images.
- For detecting blurriness, BE and BEW and CPBD perform very robustly. When images are noisy or show stripe artifacts, BEW is hardly influenced.
- Of all tested non-reference metrics, MLC and MSLC are best able to indicate ghosting artifacts.
- If normalization was used before metric assessment, the method and all relevant parameters must be reported in detail. These parameters must be considered, when comparing scores across studies, because normalization parameters can have a significant effect on absolute metric values.
- The data range parameter L is commonly used to adapt metrics, that were originally designed for a fixed 8-bit value range, to float valued images with potentially infinite intensity value ranges. However, scaling or binning to the range (0, 255) is often more consistent with the original design due to internal constants (e.g. SSIM) and thresholds (e.g. JNB). For reference metrics, the data range should be derived at least from both images if not from the whole dataset.
- For NMI and PCC, a data range parameter L is not needed and normalization can be omitted, if similar intensity values represent similar tissue types. Otherwise, an appropriate normalization method should aim for mapping similar tissue types to similar intensity values.
- If source images and target images are not spatially aligned, they must be registered with highest possible precision before evaluating with reference metrics. Rigid translation reduces assessed similarity more substantially than small local elastic deformations. CW-SSIM is robust against small translations. The type of interpolation used for registration may additionally blur the images.
- A segmentation downstream task is extremely useful for evaluation, because small but relevant structures are assessed. The performance of the segmentation model must be verified before using the segmentations for similarity assessment.

In summary, the metrics for evaluation of image-to-image MR synthesis models must be selected carefully. Frequently used SSIM and PSNR cover a large range of distortions, but have specific weaknesses, that must be covered by other metrics. Specifically PSNR does not seem appropriate for the evaluation of synthetic images. We suggest to always select metrics, that are able to detect undesired distortions specific and typical for the desired application and that are insensitive towards admitted and expected distortions. Which metrics are most appropriate can be directly derived from our experimental results. As metrics are also often used as loss functions for model training [87] or validation metrics for model selection, the choice of appropriate metrics can directly improve image synthesis models before clinical validation by human readers and thereby reduce development time and costs.

Author Contributions

M.D. and M.L. designed the study, M.D. performed the experiments, and analysed the results. All authors reviewed and contributed to the manuscript.

Additional Information

Competing interests

The authors declare no competing interests.

Data availability

The BraSyn 2023 dataset is available at www.synapse.org/brats2023.

References

1. Saharia, C. *et al.* Palette: Image-to-image diffusion models. In *ACM SIGGRAPH 2022 Conference Proceedings*, SIGGRAPH '22, DOI: [10.1145/3528233.3530757](https://doi.org/10.1145/3528233.3530757) (Association for Computing Machinery, New York, NY, USA, 2022).
2. Isola, P., Zhu, J.-Y., Zhou, T. & Efros, A. A. Image-to-image translation with conditional adversarial networks. In *2017 IEEE Conference on Computer Vision and Pattern Recognition (CVPR)*, 5967–5976, DOI: [10.1109/CVPR.2017.632](https://doi.org/10.1109/CVPR.2017.632) (2017).
3. Yi, X., Walia, E. & Babyn, P. Generative adversarial network in medical imaging: A review. *Med. Image Analysis* **58**, 101552, DOI: <https://doi.org/10.1016/j.media.2019.101552> (2019).
4. Ho, J., Jain, A. & Abbeel, P. Denoising diffusion probabilistic models. In Larochelle, H., Ranzato, M., Hadsell, R., Balcan, M. & Lin, H. (eds.) *Advances in Neural Information Processing Systems*, vol. 33, 6840–6851 (Curran Associates, Inc., 2020).
5. Müller-Franzes, G. *et al.* A multimodal comparison of latent denoising diffusion probabilistic models and generative adversarial networks for medical image synthesis. *Sci. Reports* **13**, 12098 (2023).
6. Kebaili, A., Lapuyade-Lahorgue, J. & Ruan, S. Deep Learning Approaches for Data Augmentation in Medical Imaging: A Review. *J. imaging* **9**, DOI: [10.3390/jimaging9040081](https://doi.org/10.3390/jimaging9040081) (2023). Place: Switzerland.
7. Zhu, J.-Y., Park, T., Isola, P. & Efros, A. A. Unpaired image-to-image translation using cycle-consistent adversarial networks. In *2017 IEEE International Conference on Computer Vision (ICCV)*, 2242–2251, DOI: [10.1109/ICCV.2017.244](https://doi.org/10.1109/ICCV.2017.244) (2017).
8. Kaji, S. & Kida, S. Overview of image-to-image translation by use of deep neural networks: denoising, super-resolution, modality conversion, and reconstruction in medical imaging. *Radiol. Phys. Technol.* **12**, 235–248 (2019).
9. Hong, K.-T. *et al.* Lumbar spine computed tomography to magnetic resonance imaging synthesis using generative adversarial network: Visual turing test. *Diagn. (Basel)* (2022).
10. Bahrami, A., Karimian, A. & Arabi, H. Comparison of different deep learning architectures for synthetic ct generation from mr images. *Phys. Medica* **90**, 99–107, DOI: <https://doi.org/10.1016/j.ejmp.2021.09.006> (2021).
11. Zhu, L. *et al.* Make-a-volume: Leveraging latent diffusion models for cross-modality 3d brain mri synthesis. In Greenspan, H. *et al.* (eds.) *Medical Image Computing and Computer Assisted Intervention – MICCAI 2023*, 592–601 (Springer Nature Switzerland, Cham, 2023).
12. Ben-Cohen, A., Klang, E., Raskin, S. P., Amitai, M. M. & Greenspan, H. Virtual pet images from ct data using deep convolutional networks: Initial results. In Tsafaris, S. A., Gooya, A., Frangi, A. F. & Prince, J. L. (eds.) *Simulation and Synthesis in Medical Imaging*, 49–57 (Springer International Publishing, Cham, 2017).
13. Li, Q. *et al.* Eliminating ct radiation for clinical pet examination using deep learning. *Eur. J. Radiol.* **154**, 110422 (2022).
14. Ammari, S. *et al.* Can deep learning replace gadolinium in neuro-oncology?: A reader study. *Investig. Radiol.* **57**, 99–107 (2022).
15. Baltruschat, I. M., Kreis, F., Hoelscher, A., Dohmen, M. & Lenga, M. freggan with k-space loss regularization for medical image translation. <https://arxiv.org/abs/2303.15938> (2023).
16. Weigert, M. *et al.* Content-aware image restoration: pushing the limits of fluorescence microscopy. *Nat. Methods* **15**, 1090 – 1097 (2018).
17. Lu, J., Öfverstedt, J., Lindblad, J. & Sladoje, N. Is image-to-image translation the panacea for multimodal image registration? a comparative study. *PLOS ONE* **17**, 1–33, DOI: [10.1371/journal.pone.0276196](https://doi.org/10.1371/journal.pone.0276196) (2022).
18. Raut, P., Baldini, G., Schöneck, M. & Caldeira, L. Using a generative adversarial network to generate synthetic mri images for multi-class automatic segmentation of brain tumors. *Front. Radiol.* **3**, DOI: [10.3389/fradi.2023.1336902](https://doi.org/10.3389/fradi.2023.1336902) (2024).
19. Mallio, C. A. *et al.* Artificial intelligence to reduce or eliminate the need for gadolinium-based contrast agents in brain and cardiac mri: A literature review. *Investig. Radiol.* **58** (2023).
20. Borji, A. Pros and cons of gan evaluation measures: New developments. *Comput. Vis. Image Underst.* **215**, 103329, DOI: <https://doi.org/10.1016/j.cviu.2021.103329> (2022).
21. Salimans, T. *et al.* Improved techniques for training gans. *CoRR abs/1606.03498* (2016). [1606.03498](https://doi.org/10.4236/ojs.2016063498).

22. Heusel, M., Ramsauer, H., Unterthiner, T., Nessler, B. & Hochreiter, S. Gans trained by a two time-scale update rule converge to a local nash equilibrium. In *Proceedings of the 31st International Conference on Neural Information Processing Systems*, NIPS'17, 6629–6640 (Curran Associates Inc., Red Hook, NY, USA, 2017).
23. Crété-Roffet, F., Dolmire, T., Ladret, P. & Nicolas, M. The Blur Effect: Perception and Estimation with a New No-Reference Perceptual Blur Metric. In *SPIE Electronic Imaging Symposium Conf Human Vision and Electronic Imaging*, vol. XII, EI 6492–16 (San Jose, United States, 2007).
24. Shurcliff, W. A. Studies in optics: A.a. michelson, university of chicago press, 1927, republished in 1962 as phoenix science series no. 514 paperback, 176 pp. illustrated, \$1.75. *J. Phys. Chem. Solids* **24**, 498–499 (1963).
25. Rudin, L. I., Osher, S. & Fatemi, E. Nonlinear total variation based noise removal algorithms. *Phys. D: Nonlinear Phenom.* **60**, 259–268, DOI: [https://doi.org/10.1016/0167-2789\(92\)90242-F](https://doi.org/10.1016/0167-2789(92)90242-F) (1992).
26. Pianykh, O. S., Pospelova, K. & Kamboj, N. H. Modeling human perception of image quality. *J. Digit. Imaging* **31**, 768–775 (2018).
27. Ponomarenko, N. *et al.* A new color image database tid2013: Innovations and results. In Blanc-Talon, J., Kasinski, A., Philips, W., Popescu, D. & Scheunders, P. (eds.) *Advanced Concepts for Intelligent Vision Systems*, 402–413 (Springer International Publishing, Cham, 2013).
28. Sheikh, H., Sabir, M. & Bovik, A. A statistical evaluation of recent full reference image quality assessment algorithms. *IEEE Transactions on Image Process.* **15**, 3440–3451, DOI: [10.1109/TIP.2006.881959](https://doi.org/10.1109/TIP.2006.881959) (2006).
29. Sheikh, H., Wang, Z., Cormack, L. & Bovik, A. Live image quality assessment database release 2. <http://live.ece.utexas.edu/research/quality>.
30. Chow, L. S., Rajagopal, H. & Paramesran, R. Correlation between subjective and objective assessment of magnetic resonance (mr) images. *Magn. Reson. Imaging* **34**, 820–831, DOI: <https://doi.org/10.1016/j.mri.2016.03.006> (2016).
31. International Medical Device Regulators Forum. Software as a medical device (samd): Clinical evaluation - guidance for industry and food and drug administration staff. <https://www.fda.gov/regulatory-information/search-fda-guidance-documents/software-medical-device-samd-clinical-evaluation> (2017).
32. Cruz Rivera, S. *et al.* Guidelines for clinical trial protocols for interventions involving artificial intelligence: the spirit-ai extension. *The Lancet. Digit. health* **2**, e549–e560 (2020).
33. Kim, D. W., Jang, H. Y., Kim, K. W., Shin, Y. & Park, S. H. Design characteristics of studies reporting the performance of artificial intelligence algorithms for diagnostic analysis of medical images: Results from recently published papers. *Korean journal radiology* **20**, 405–410 (2019).
34. Liu, X. *et al.* A comparison of deep learning performance against health-care professionals in detecting diseases from medical imaging: a systematic review and meta-analysis. *The Lancet Digit. Heal.* **1**, e271–e297, DOI: [https://doi.org/10.1016/S2589-7500\(19\)30123-2](https://doi.org/10.1016/S2589-7500(19)30123-2) (2019).
35. Khunte, M. *et al.* Trends in clinical validation and usage of us food and drug administration-cleared artificial intelligence algorithms for medical imaging. *Clin. Radiol.* **78**, 123–129, DOI: <https://doi.org/10.1016/j.crad.2022.09.122> (2023). Special Issue Section: Artificial Intelligence and Machine Learning.
36. Nagendran, M. *et al.* Artificial intelligence versus clinicians: systematic review of design, reporting standards, and claims of deep learning studies. *BMJ* **368**, DOI: [10.1136/bmj.m689](https://doi.org/10.1136/bmj.m689) (2020). <https://www.bmjjournals.org/content/368/bmj.m689.full.pdf>.
37. Yasui, K. *et al.* Validation of deep learning-based ct image reconstruction for treatment planning. *Sci. Reports* **13**, 15413 (2023).
38. Bonardel, G. *et al.* Clinical and phantom validation of a deep learning based denoising algorithm for f-18-fdg pet images from lower detection counting in comparison with the standard acquisition. *EJNMMI Phys.* **9**, 36 (2022).
39. Food and Drug Administration (FDA). Artificial intelligence and machine learning (ai/ml)-enabled medical devices. <https://www.fda.gov/medical-devices/software-medical-device-samd/artificial-intelligence-and-machine-learning-ai/ml-enabled-medical-devices>, accessed March 14th, 2024.
40. Reinke et al., A. Understanding metric-related pitfalls in image analysis validation. *Nat. Methods* **21**, 82 – 194 (2024).
41. Maier-Hein et al., L. Metrics reloaded: recommendations for image analysis validation. *Nat. Methods* **21**, 195–212 (2024).
42. Baltruschat, I. M., Janbakhshi, P. & Lenga, M. Brasyn 2023 challenge: Missing mri synthesis and the effect of different learning objectives (2024). [2403.07800](https://doi.org/10.4236/ojs.20240402407800).
43. Nečasová, T., Burgos, N. & Svoboda, D. Validation and evaluation metrics for medical and biomedical image synthesis. In Burgos, N. & Svoboda, D. (eds.) *Biomedical Image Synthesis and Simulation*, The MICCAI Society Book Series, chap. 25, 573–600 (Academic Press, 2022).
44. McNaughton, J. *et al.* Machine learning for medical image translation: A systematic review. *Bioengineering* **10** (2023).
45. Haase, R. *et al.* Artificial contrast: Deep learning for reducing gadolinium-based contrast agents in neuroradiology. *Investig. Radiol.* **58**, 539–547 (2023).

46. Mudeng, V., Kim, M. & Choe, S.-w. Prospects of structural similarity index for medical image analysis. *Appl. Sci.* **12** (2022).
47. Huynh-Thu, Q. & Ghanbari, M. Scope of validity of psnr in image/video quality assessment. *Electron. Lett.* **44**, 800–801 (2008).
48. Korhonen, J. & You, J. Peak signal-to-noise ratio revisited: Is simple beautiful? In *2012 Fourth International Workshop on Quality of Multimedia Experience*, 37–38, DOI: [10.1109/QoMEX.2012.6263880](https://doi.org/10.1109/QoMEX.2012.6263880) (2012).
49. Wang, Z. & Bovik, A. C. Mean squared error: Love it or leave it? a new look at signal fidelity measures. *IEEE Signal Process. Mag.* **26**, 98–117, DOI: [10.1109/MSP.2008.930649](https://doi.org/10.1109/MSP.2008.930649) (2009).
50. Gourdeau, D., Duchesne, S. & Archambault, L. On the proper use of structural similarity for the robust evaluation of medical image synthesis models. *Med. Phys.* **49**, 2462–2474, DOI: <https://doi.org/10.1002/mp.15514> (2022). <https://aapm.onlinelibrary.wiley.com/doi/pdf/10.1002/mp.15514>.
51. Baker, A. H., Pinard, A. & Hammerling, D. M. On a structural similarity index approach for floating-point data. *IEEE Transactions on Vis. Comput. Graph.* 1–13, DOI: [10.1109/TVCG.2023.3332843](https://doi.org/10.1109/TVCG.2023.3332843) (2023).
52. Goodfellow, I., Bengio, Y. & Courville, A. *Deep Learning*, chap. 12.2.1 Preprocessing, 448 (MIT Press, 2016). <http://www.deeplearningbook.org>.
53. Tellez, D. *et al.* Quantifying the effects of data augmentation and stain color normalization in convolutional neural networks for computational pathology. *Med. Image Analysis* **58**, 101544, DOI: <https://doi.org/10.1016/j.media.2019.101544> (2019).
54. Onofrey, J. A. *et al.* Generalizable multi-site training and testing of deep neural networks using image normalization. *Proceedings. IEEE Int. Symp. on Biomed. Imaging* 348–351 (2019).
55. Reinhold, J. C., Dewey, B. E., Carass, A. & Prince, J. L. Evaluating the impact of intensity normalization on MR image synthesis. In Angelini, E. D. & Landman, B. A. (eds.) *Medical Imaging 2019: Image Processing*, vol. 10949, 109493H, DOI: [10.1117/12.2513089](https://doi.org/10.1117/12.2513089). International Society for Optics and Photonics (SPIE, 2019).
56. Haase, R. *et al.* Reduction of gadolinium-based contrast agents in mri using convolutional neural networks and different input protocols: Limited interchangeability of synthesized sequences with original full-dose images despite excellent quantitative performance. *Investig. Radiol.* **58** (2023).
57. Shinohara, R. T. *et al.* Statistical normalization techniques for magnetic resonance imaging. *NeuroImage: Clin.* **6**, 9–19 (2014).
58. Nyúl, L. G. & Udupa, J. K. On standardizing the mr image intensity scale. *Magn. Reson. Medicine* **42**, 1072–1081 (1999).
59. Hänsch, A., Chlebus, G., Meine, H. & *et al.* Improving automatic liver tumor segmentation in late-phase mri using multi-model training and 3d convolutional neural networks. *Sci. Reports* **12**, DOI: <https://doi.org/10.1038/s41598-022-16388-9> (2022).
60. McCormick, M., Liu, X., Ibanez, L., Jomier, J. & Marion, C. Itk: enabling reproducible research and open science. *Front. Neuroinformatics* **8**, DOI: [10.3389/fninf.2014.00013](https://doi.org/10.3389/fninf.2014.00013) (2014).
61. Numpy Developers. The fundamental package for scientific computing with python. <https://numpy.org/>.
62. Pedregosa, F. *et al.* Scikit-learn: Machine learning in Python. *J. Mach. Learn. Res.* **12**, 2825–2830 (2011).
63. van der Walt, S. *et al.* scikit-image: image processing in Python. *PeerJ* **2**, e453, DOI: [10.7717/peerj.453](https://doi.org/10.7717/peerj.453) (2014).
64. Torchmetrics - measuring reproducibility in pytorch, DOI: [10.21105/joss.04101](https://doi.org/10.21105/joss.04101) (2022).
65. Wang, Z., Bovik, A. C., Sheikh, H. R. & Simoncelli, E. P. Image quality assessment: from error visibility to structural similarity. *IEEE Transactions on Image Process.* **13**, 600–12 (2004).
66. Wang, Z., Simoncelli, E. & Bovik, A. Multiscale structural similarity for image quality assessment. In *The Thirty-Seventh Asilomar Conference on Signals, Systems and Computers, 2003*, vol. 2, 1398–1402 Vol.2, DOI: [10.1109/ACSSC.2003.1292216](https://doi.org/10.1109/ACSSC.2003.1292216) (2003).
67. Ding, K. Iqa optimization. <https://github.com/dingkeyan93/IQA-optimization/> (2020).
68. Sampat, M. P., Wang, Z., Gupta, S., Bovik, A. C. & Markey, M. K. Complex wavelet structural similarity: A new image similarity index. *IEEE Transactions on Image Process.* **18**, 2385–2401, DOI: [10.1109/TIP.2009.2025923](https://doi.org/10.1109/TIP.2009.2025923) (2009).
69. Huynh-Thu, Q. & Ghanbari, M. Scope of validity of psnr in image/video quality assessment. *Electron. Lett.* **44**, 800–801(1) (2008).
70. Perceptual similarity metric and dataset. <https://pypi.org/project/lpip/>.
71. Zhang, R., Isola, P., Efros, A. A., Shechtman, E. & Wang, O. The unreasonable effectiveness of deep features as a perceptual metric. *CoRR* **1801.03924** (2018). [1801.03924](https://arxiv.org/abs/1801.03924).
72. Ding, K. <https://github.com/dingkeyan93/DISTS>.
73. Ding, K., Ma, K., Wang, S. & Simoncelli, E. P. Image quality assessment: Unifying structure and texture similarity. *IEEE Transactions on Pattern Analysis Mach. Intell.* **44**, 2567–2581, DOI: [10.1109/TPAMI.2020.3045810](https://doi.org/10.1109/TPAMI.2020.3045810) (2022).
74. Choi, M. G., Jung, J. H. & Jeon, J. W. No-reference image quality assessment using blur and noise. *Int. J. Electr. Comput. Eng.* **3**, 184–188 (2009).

75. Pech-Pacheco, J., Cristobal, G., Chamorro-Martinez, J. & Fernandez-Valdivia, J. Diatom autofocusing in brightfield microscopy: a comparative study. In *Proceedings 15th International Conference on Pattern Recognition. ICPR-2000*, vol. 3, 314–317 vol.3, DOI: [10.1109/ICPR.2000.903548](https://doi.org/10.1109/ICPR.2000.903548) (2000).

76. Marziliano, P., Dufaux, F., Winkler, S. & Ebrahimi, T. A no-reference perceptual blur metric. In *Proceedings. International Conference on Image Processing*, vol. 3, III–III, DOI: [10.1109/ICIP.2002.1038902](https://doi.org/10.1109/ICIP.2002.1038902) (2002).

77. Roberts, D. <https://github.com/davidatroborts/No-Reference-Sharpness-Metric>.

78. Ferzli, R. & Karam, L. J. A no-reference objective image sharpness metric based on the notion of just noticeable blur (jnb). *IEEE Transactions on Image Process.* **18**, 717–728, DOI: [10.1109/TIP.2008.2011760](https://doi.org/10.1109/TIP.2008.2011760) (2009).

79. Karam, L. & Narvekar, N. <https://github.com/0x64746b/python-cpbd>.

80. Narvekar, N. D. & Karam, L. J. A no-reference image blur metric based on the cumulative probability of blur detection (cpbd). *IEEE Transactions on Image Process.* **20**, 2678–2683, DOI: [10.1109/TIP.2011.2131660](https://doi.org/10.1109/TIP.2011.2131660) (2011).

81. Schuppert et al., C. Whole-body magnetic resonance imaging in the large population-based german national cohort study: Predictive capability of automated image quality assessment for protocol repetitions. *Investig. Radiol.* **57** (2022).

82. Guha, R. <https://pypi.org/project/brisque>.

83. Mittal, A., Moorthy, A. K. & Bovik, A. C. No-reference image quality assessment in the spatial domain. *IEEE Transactions on Image Process.* **21**, 4695–4708, DOI: [10.1109/TIP.2012.2214050](https://doi.org/10.1109/TIP.2012.2214050) (2012).

84. Gupta, P. <https://github.com/guptapraful/niqe>.

85. Mittal, A., Soundararajan, R. & Bovik, A. C. Making a “completely blind” image quality analyzer. *IEEE Signal Process. Lett.* **20**, 209–212, DOI: [10.1109/LSP.2012.2227726](https://doi.org/10.1109/LSP.2012.2227726) (2013).

86. Li, Y. et al. Samscore: A semantic structural similarity metric for image translation evaluation (2023). [2305.15367](https://doi.org/10.4236/230515367).

87. Ding, K., Ma, K., Wang, S. & Simoncelli, E. P. Comparison of image quality models for optimization of image processing systems. *CoRR* **abs/2005.01338** (2020).

88. Liu, J. et al. One model to synthesize them all: Multi-contrast multi-scale transformer for missing data imputation. *IEEE Transactions on Med. Imaging* **42**, 2577–2591, DOI: [10.1109/TMI.2023.3261707](https://doi.org/10.1109/TMI.2023.3261707) (2023).

89. Hénaff, O. J. & Simoncelli, E. P. Geodesics of learned representations. *Proc. Int. Conf. Learn. Represent.* 1–10 (2016).

90. Maes, F., Collignon, A., Vandermeulen, D., Marchal, G. & Suetens, P. Multimodality image registration by maximization of mutual information. *IEEE Transactions on Med. Imaging* **16**, 187–198, DOI: [10.1109/42.563664](https://doi.org/10.1109/42.563664) (1997).

91. Ghorbani, A., Natarajan, V., Coz, D. & Liu, Y. DermGAN: Synthetic Generation of Clinical Skin Images with Pathology. In Dalca, A. V. et al. (eds.) *Proceedings of the Machine Learning for Health NeurIPS Workshop*, vol. 116 of *Proceedings of Machine Learning Research*, 155–170 (PMLR, 2020).

92. Jang, M. et al. Image turing test and its applications on synthetic chest radiographs by using the progressive growing generative adversarial network. *Sci. Reports* **13** (2023).

93. McNaughton, J. et al. Synthetic mri generation from ct scans for stroke patients. *BioMedInformatics* **3**, 791–816, DOI: [10.3390/biomedinformatics3030050](https://doi.org/10.3390/biomedinformatics3030050) (2023).

94. Zimmermann, L. et al. An mri sequence independent convolutional neural network for synthetic head ct generation in proton therapy. *Zeitschrift fuer Medizinische Physik* **32**, 218–227 (2022).

95. Xing, X., Nan, Y., Felder, F., Walsh, S. & Yang, G. The beauty or the beast: Which aspect of synthetic medical images deserves our focus? In *2023 IEEE 36th International Symposium on Computer-Based Medical Systems (CBMS)*, 523–528, DOI: [10.1109/CBMS58004.2023.00273](https://doi.org/10.1109/CBMS58004.2023.00273) (IEEE Computer Society, Los Alamitos, CA, USA, 2023).

96. Dice, L. R. Measures of the amount of ecologic association between species. *Ecology* **26**, 297–302, DOI: <https://doi.org/10.2307/1932409> (1945).

97. Mason, A. et al. Comparison of objective image quality metrics to expert radiologists’ scoring of diagnostic quality of mr images. *IEEE Transactions on Med. Imaging* **39**, 1064–1072, DOI: [10.1109/TMI.2019.2930338](https://doi.org/10.1109/TMI.2019.2930338) (2020).

98. Jayachandran Preetha, C. et al. Deep-learning-based synthesis of post-contrast t1-weighted mri for tumour response assessment in neuro-oncology: a multicentre, retrospective cohort study. *The Lancet Digit. Heal.* **3**, e784–e794, DOI: [https://doi.org/10.1016/S2589-7500\(21\)00205-3](https://doi.org/10.1016/S2589-7500(21)00205-3) (2021).

99. Zhu, M., Yu, L., Wang, Z., Ke, Z. & Zhi, C. Review: A survey on objective evaluation of image sharpness. *Appl. Sci.* **13**, DOI: [10.3390/app13042652](https://doi.org/10.3390/app13042652) (2023).

100. Canny, J. A computational approach to edge detection. *IEEE Transactions on Pattern Analysis Mach. Intell. PAMI* **8**, 679–698, DOI: [10.1109/TPAMI.1986.4767851](https://doi.org/10.1109/TPAMI.1986.4767851) (1986).

101. Martin, D., Fowlkes, C., Tal, D. & Malik, J. A database of human segmented natural images and its application to evaluating segmentation algorithms and measuring ecological statistics. In *Proceedings Eighth IEEE International Conference on Computer Vision. ICCV 2001*, vol. 2, 416–423 vol.2, DOI: [10.1109/ICCV.2001.937655](https://doi.org/10.1109/ICCV.2001.937655) (2001).

102. Li, H. B. & et al. The brain tumor segmentation (brats) challenge 2023: Brain mr image synthesis for tumor segmentation brasyn. <https://arxiv.org/abs/2305.09011> (2023).

103. Consortium, M. Monai: Medical open network for ai (2023). <https://docs.monai.io/en/stable/auto3dseg.html>.
104. Cohen, J. P., Luck, M. & Honari, S. Distribution matching losses can hallucinate features in medical image translation. In Frangi, A. F., Schnabel, J. A., Davatzikos, C., Alberola-López, C. & Fichtinger, G. (eds.) *Medical Image Computing and Computer Assisted Intervention – MICCAI 2018*, 529–536 (Springer International Publishing, Cham, 2018).
105. Liu, J. *et al.* Dyefreenet: Deep virtual contrast ct synthesis. In Burgos, N., Svoboda, D., Wolterink, J. M. & Zhao, C. (eds.) *Simulation and Synthesis in Medical Imaging*, 80–89 (Springer International Publishing, Cham, 2020).
106. Dohmen, M., Truong, T., Baltruschat, I. M. & Lenga, M. Five pitfalls when assessing synthetic medical images with reference metrics (2024). <https://arxiv.org/abs/2408.06075>, accepted at Deep Generative Models workshop at MICCAI 2024.
107. Tustison, N. J. *et al.* N4itk: improved n3 bias correction. *IEEE transactions on medical imaging* **29**, 1310–20 (2010).

Supplement

A Supplemental Methods

A.1 Notation

Let I be an image with intensity $I(\mathbf{x})$ at pixel location \mathbf{x} . A three-dimensional image $I \in \mathbb{R}^{h \times w \times d}$ of height h , width w and depth d consists of $|I| = h \cdot w \cdot d$ pixels, with pixel locations denoted as $\mathbf{x} = (x_1, x_2, x_3) \in \mathbb{N}^3$ with $0 \leq x_1 < h$, $0 \leq x_2 < w$, $0 \leq x_3 < d$. Accordingly, a two-dimensional image is defined as $I \in \mathbb{R}^{h \times w}$ with pixel locations $\mathbf{x} = (x_1, x_2)$ and $|I| = h \cdot w$ pixels in total. Let I_{\max} denote the maximum intensity, I_{\min} the minimum intensity, μ_I the mean intensity, σ_I the standard deviation of all image intensities in I . The k -th percentile $I_{k\%} \in \mathbb{R}$ of the image I is the smallest intensity value, such that a fraction of $k\%$ of all pixels in I have lower or equal intensity value. The median of all image intensities in I is $I_{50\%}$. The interquartile range (IQR) is $I_{75\%} - I_{25\%}$.

A.2 Calculation of Normalization Methods

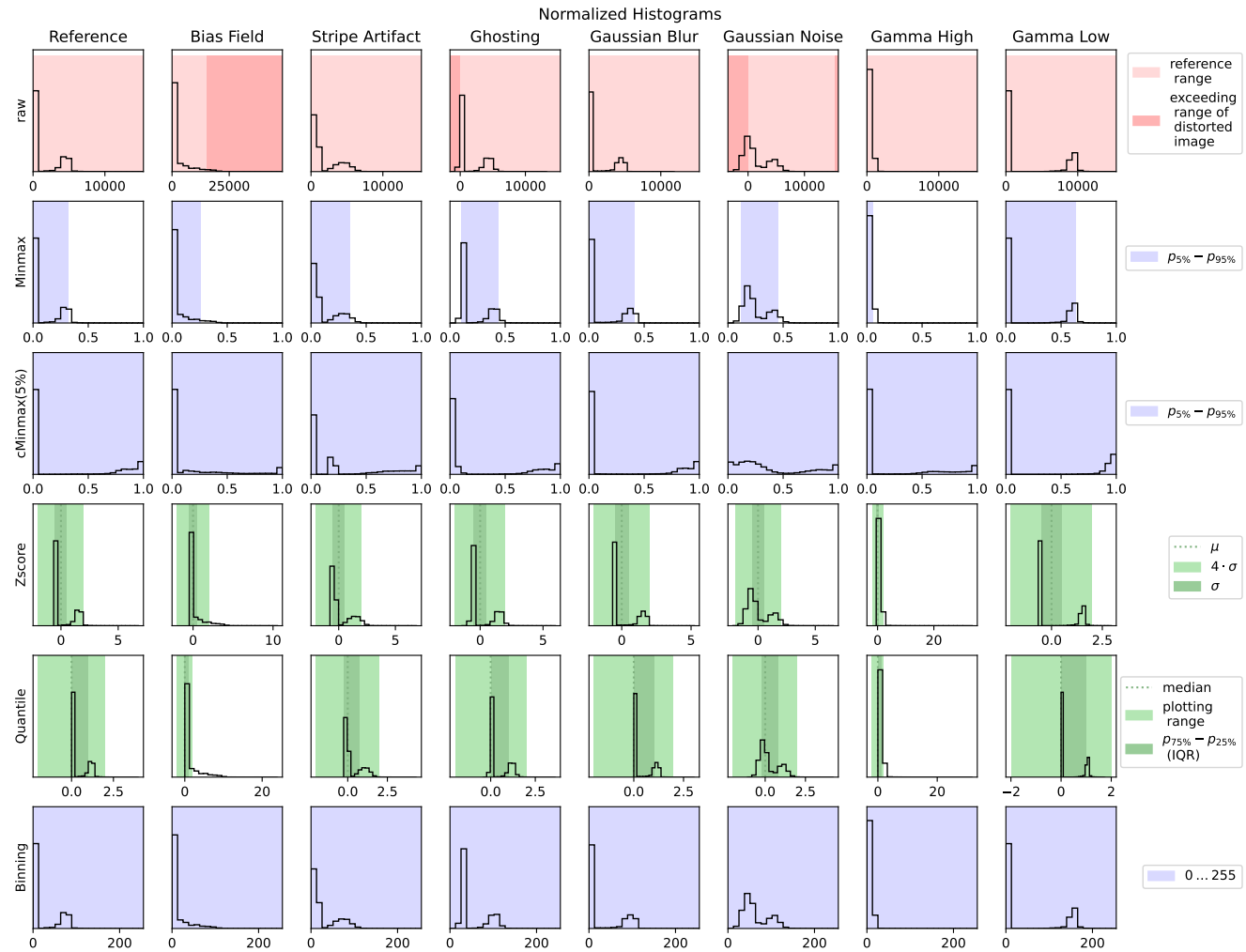


Figure S.1. Normalized histograms of reference distorted images. In the first row, unnormalized raw reference image (first column) and different distortions applied with highest strength (5/5). The shape, position and/or the intensity value range of the histogram changes with the selected distortions. Exceeding value ranges are highlighted with a darker compared to the lighter pink shade of the reference image value range. Minmax normalization scales the x-axis to a $[0, 1]$ range, while cMinmax significantly changes the histogram shape by clipping outliers and stretching the rest of the histogram. Zscore and Quantile normalization are similar, but in these images, the mean is higher than the median, and the interquartile range (IQR) is smaller, than the standard deviation.

The calculation for all normalization methods is found [here](#).

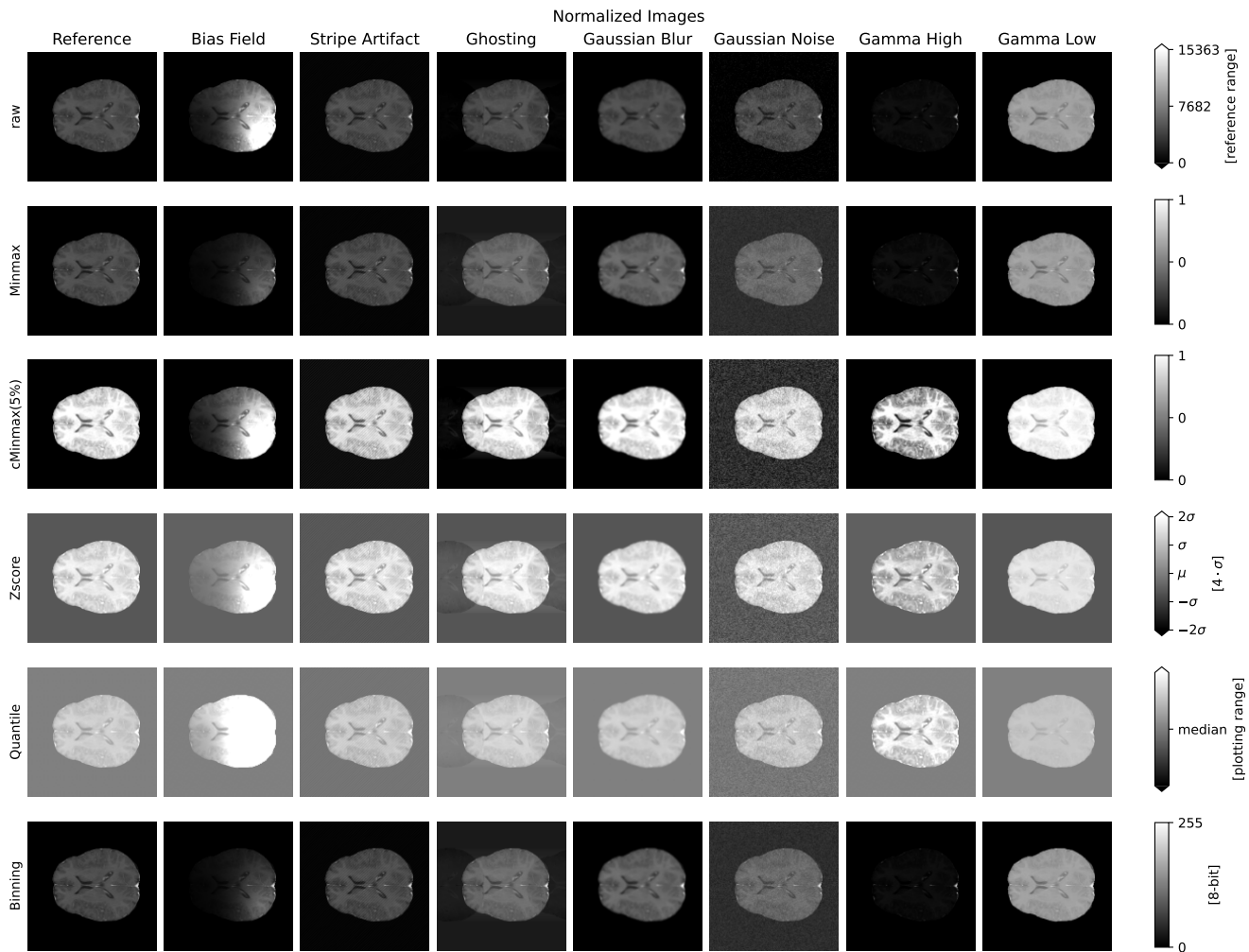


Figure S.2. Normalized reference and distorted images. In the first row, unnormalized raw reference image (first column) and different distortions applied with highest strength (5/5). The visualized range in the first row is restricted to the intensity range of the reference image. The second row, showing Minmax normalized images visualizes the full intensity range. Images normalized with cMinmax in the third row appear with higher contrast, because the intensity range is clipped at 5% and 95%. Zscore and Quantile yield similar result, but in these images, the mean is higher than the median, and the interquartile range (IQR) is smaller, than the standard deviation. Therefore, the Zscore normalized images appear darker in the background and with more contrast in the plotted intensity range [-2, 2] compared to the Quantile normalized images, which appear brighter in the background and with less contrast in the plotted intensity range [-2,2].

Minmax

Given a (sub-) intensity range $[i_1, i_2]$ the image intensities are shifted and scaled to meet a target intensity range $[j_1, j_2]$. For the default choice of $i_1 = I_{\min}$, $i_2 = I_{\max}$, $j_1 = 0$ and $j_2 = 1$, these parameters are dropped.

$$\text{Minmax}_{[i_1, i_2] \rightarrow [j_1, j_2]}(I) = \frac{I - i_1}{i_2 - i_1} \cdot (j_2 - j_1) + j_1 \quad \text{Minmax}(I) = \frac{I - I_{\min}}{I_{\max} - I_{\min}} \quad (1)$$

In case of constant images with $I_{\min} = I_{\max}$, the division by zero is omitted, such that the result is a constant image $\text{Minmax}(I) = j_1$.

cMinmax

Clipped Minmax normalization is equal to Minmax normalization with previous clipping at the percentiles $I_{p\%}$ and $I_{q\%}$. If only $p < 50\%$ is given, the default is $q = 100\% - p = 95$ and $j_1 = 0$ and $j_2 = 1$, which reduces the notation.

$$\text{cMinmax}_{[I_{p\%}, I_{q\%}] \rightarrow [j_1, j_2]}(I) = \text{Minmax}_{[I_{p\%}, I_{q\%}] \rightarrow [j_1, j_2]}((\text{clip}_{I_{p\%}, I_{q\%}}(I))) \quad \text{clip}_{[I_{p\%}, I_{q\%}]}(I) = \begin{cases} I_{p\%} & , \text{if } I(\mathbf{x}) \leq I_{p\%} \\ I_{q\%} & , \text{if } I(\mathbf{x}) \geq I_{q\%} \\ I(\mathbf{x}) & , \text{else} \end{cases} \quad (2)$$

$$\text{cMinmax}_{p\%}(I) = \text{Minmax}(\text{clip}_{[I_{p\%}, I_{100\%-p\%}]}(I))$$

In case of (nearly) constant images with $I_{p\%} = I_{q\%}$, the result becomes a constant image with $\text{cMinmax}(I) = j_1$.

Zscore

$$\text{Zscore}(I) = \frac{I - \mu_I}{\sigma_I} \quad (3)$$

In case of constant images with $\sigma_I = 0$, the division by zero is omitted, such that $\text{ZScore}(I) = 0$.

Quantile

$$\text{Quantile}(I) = \frac{I - I_{50\%}}{I_{75\%} - I_{25\%}} \quad (4)$$

In case of a large fraction of equal image values, i.e. $I_{25\%} = I_{75\%}$, the division by zero is omitted, such that $\text{Quantile}(I) = I - I_{50\%}$.

Binning

The image intensities are mapped to B bin values.

$$\text{Bin}_B(I) = \min(B - 1, \lfloor \text{Minmax}_{[I_{\min}, I_{\max}] \rightarrow [0, B-1]} \rfloor) = \min(B - 1, \lfloor B \cdot (I - I_{\min}) / (I_{\max} - I_{\min}) \rfloor) \quad (5)$$

A.3 Metric Calculation

Reference and non-reference metrics are ordered alphabetically.

BE (Blur-Effect)

For each dimension $d = 1, \dots, n$ of I , a blurred version \tilde{I} of image I is created by convolution with a uniform kernel $U_{k,d}$ of size k along d . The absolute differences of neighboring pixels along d are in \tilde{I} and I as \tilde{D} and D respectively. D_d and \tilde{D}_d can be seen as the gradients or edge images of the original image I and its blurred version \tilde{I} . Then the sum of positive differences $D - \tilde{D}$ is related to the sum of differences D only as a measure of blurriness. BE is implemented in the scikit-image python library [63] with a default of $k = 11$. In detail, we compute for all d :

$$\begin{aligned} \tilde{I}_d &= \text{conv}(U_{k,d}, I) \\ D_d &= |\nabla_d(I)| \quad S_d = \sum_{\mathbf{x}} D_d(\mathbf{x}) \\ \tilde{D}_d &= |\nabla_d(\tilde{I}_d)| \quad \tilde{S}_d = \sum_{\mathbf{x}} \max(0, D_d(\mathbf{x}) - \tilde{D}_d(\mathbf{x})) \end{aligned} \quad (6)$$

where $\nabla_d(I)$ denotes the differential of image I in dimension d and \mathbf{x} denotes all pixel locations in D_d . The final Blur-Effect is defined as

$$\text{BE} = \max_d \frac{S_d - \tilde{S}_d}{S_d} \quad (7)$$

BEW (Blurred Edge Widths)

First, edge pixels are detected along all dimensions d as $E_d(\mathbf{x}) = 1$ and non-edge pixels as $E_d(\mathbf{x}) = 0$, e.g. with the canny algorithm [100]. Second, edge pixels are traced along their detected dimension to find the next pixel with a differently signed gradient, which marks the end of the edge. The summed distances of the edge pixel to the ends of the edge determine the edge width $W_d(\mathbf{x})$ for dimension d .

Let d be a number of dimensions $\in 0, 1, \dots, n$, then the BEW metric is defined as:

$$\text{BEW}(\mathbf{x}) = \frac{1}{n} \cdot \sum_d \frac{\sum_{\mathbf{x}} W_d(\mathbf{x})}{\sum_{\mathbf{x}} E_d(\mathbf{x})} \quad (8)$$

BR (Blur Ratio)

In order to identify edge pixels, the image gradient along dimension d and the mean absolute value μ_{D_d} are computed:

$$D_d = |\nabla_d(I)| \quad \mu_{D_d} = \frac{1}{|I|} \sum_{\mathbf{x}} D_d(\mathbf{x}) \quad (9)$$

With two further criteria, a binary map of edge pixels $E_d(\mathbf{x}) \in \{0, 1\}$ is derived from D_d . First, all pixels with gradient values lower or equal to the mean gradient are set to 0 in the edge candidate gradient map C_d . Second, the gradient value must exceed the values of its direct neighbors in dimension d :

$$C_d(\mathbf{x}) = \begin{cases} D_d(\mathbf{x}) & , \text{if } D_d(\mathbf{x}) > \mu_{D_d} \\ 0 & , \text{otherwise} \end{cases} \quad E_d(\mathbf{x}) = \begin{cases} 1 & , \text{if } C_d(\mathbf{x}) > C_d(\mathbf{x}_1, \dots, \mathbf{x}_d + 1, \dots, \mathbf{x}_n) \\ & \text{and } C_d(\mathbf{x}) > C_d(\mathbf{x}_1, \dots, \mathbf{x}_d - 1, \dots, \mathbf{x}_n) \\ 0 & , \text{otherwise} \end{cases} \quad (10)$$

In order to determine blurred pixels, the average intensity $A_d(\mathbf{x})$ of the neighbors of \mathbf{x} in dimension d is defined.

$$A_d(\mathbf{x}) = \frac{|I(x_1, \dots, x_d - 1, \dots, x_n) - I(x_1, \dots, x_d + 1, \dots, x_n)|}{2} \quad (11)$$

And then related to the pixel intensity to define the inverse blurriness IB_d for dimension d . A threshold t_{IB} identifies blurred pixels, where the inverse blurriness of all dimensions d falls below t_{BR} .

$$IB_d(\mathbf{x}) = \frac{|I(\mathbf{x}) - A_d(\mathbf{x})|}{A_d(\mathbf{x})} \quad B(\mathbf{x}) = \begin{cases} 1 & , \text{if } \max_d(IB_d(\mathbf{x})) < t_{IB} \\ 0 & , \text{otherwise} \end{cases} \quad (12)$$

$$\text{BR} = \frac{\sum_{\mathbf{x}} B(\mathbf{x})}{\sum_{\mathbf{x}} \max_d(E_d(\mathbf{x}))} \quad \text{MB} = \frac{\sum_{\mathbf{x}} \max_d IB_d(\mathbf{x})}{\sum_{\mathbf{x}} B(\mathbf{x})}$$

Based on experiments, the original paper proposes a threshold of $t_{IB} = 0.1$. The BR metric is defined as the ratio of the total number of blurred pixels and the total number of edge pixels

BRISQUE (Blind/Reference-less Image Spatial Quality Evaluator)

As a first step, the image I is normalized with a modified zscore method [83] including a stabilizing constant $C = 1$ to I' , also called mean subtracted contrast normalized (MSCN) coefficients.

$$I' = \frac{I - \hat{\mu}_I}{\hat{\sigma}_I + C} \quad (13)$$

In a second step, pairwise products of image intensities in a direct neighborhood are calculated:

$$\begin{aligned} H(I', \mathbf{x}) &= I'(\mathbf{x}) \cdot I'(x_1 + 1, x_2) & (\text{horizontal}) \\ V(I', \mathbf{x}) &= I'(\mathbf{x}) \cdot I'(x_1, x_2 + 1) & (\text{vertical}) \\ D_1(I', \mathbf{x}) &= I'(\mathbf{x}) \cdot I'(x_1 + 1, x_2 + 1) & (\text{first diagonal}) \\ D_2(I', \mathbf{x}) &= I'(\mathbf{x}) \cdot I'(x_1 - 1, x_2 + 1) & (\text{second diagonal}) \end{aligned} \quad (14)$$

Third, a general Gaussian distribution is fitted to I' with parameters shape s and variance v as well as asymmetric Gaussian distributions are fitted to each of H , V , D_1 and D_2 with parameters shape s , mean m , left variance lv , and right variance rv , yielding $1 \cdot 2 + 4 \cdot 4 = 18$ parameters. Finally, the BRISQUE quality score is predicted from these features by a trained support vector regressor.

CW-SSIM (Complex-Wavelet Structural Similarity Index Measure)

In the complex wavelet transform domain, suppose $\mathbf{c}_{\mathbf{x},i} = \{c_{\mathbf{x},i} | i = 1, N\}$ and $\mathbf{d}_{\mathbf{x},i} = \{d_{\mathbf{x},i} | i = 1, N\}$ are two sets of coefficients extracted at the same spatial location \mathbf{x} in the same wavelet subbands of the two images I and R being compared, respectively. Then, CW-SSIM is defined as

$$\text{CW-SSIM}(I, R) = \frac{1}{|I|} \sum_{\mathbf{x} \in R} \frac{2 |\sum_{i=1}^N c_{\mathbf{x},i} \cdot d_{\mathbf{x},i}^*| + K}{\sum_{i=1}^N |c_{\mathbf{x},i}|^2 + \sum_{i=1}^N |d_{\mathbf{x},i}|^2 + K} \quad (15)$$

where $d_{\mathbf{x},i}^*$ is the complex conjugate of $d_{\mathbf{x},i}$ and K is a constant to improve robustness, where the local signal-to-noise ratios are low. For our experiments, we used an implementation[67] with $K = 1 \cdot 10^{-12}$ and images were Minmax normalized to range $(0, 255)$.

CPBD (Cumulative Probability of Blur Detection)

The probability of detecting blur in a pixel \mathbf{x} of an edge block e can be expressed as an exponential function of $p(\mathbf{x}, e)$. Let \mathcal{X} be the set of processed edge pixels, i.e. the set of detected edge pixels located in an edge block $e \in \mathcal{E}$. Then the CPBD metric corresponds to the cumulative probability of detecting blur in any of the processed edge pixels with a probability ≤ 0.63 .

$$p(\mathbf{x}, e) = 1 - \exp \left(- \left| \frac{W_0(\mathbf{x})}{\text{jnb}(e, L)} \right| \right)^\beta \quad \mathcal{X} := \left\{ \mathbf{x} \mid \max_d E_d(\mathbf{x}) = 1 \wedge \exists e \in \mathcal{E} : \mathbf{x} \in e \right\} \quad (16)$$

$$\text{CPBD}(I) = \sum_{\mathbf{x} \in \mathcal{X}} \begin{cases} 1/|\mathcal{X}| & , \text{if } p(\mathbf{x}, e) \leq 0.63 \\ 0 & , \text{else} \end{cases} \quad (17)$$

We employed canny edge detection with a lower threshold at $0.1 \cdot L$ and a higher threshold of $0.2 \cdot L$, and scaled $\text{jnb}(e)$ with L as defined in Eq. (21).

DICE

For segmentations S_I and S_R of images I and R respectively, the DICE score relates the intersection of both segmentations to the sum of their sizes.

$$\text{DICE}(S_I, S_R) = \frac{2|S_I \cap S_R| + \epsilon}{|S_I| + |S_R| + \epsilon} \quad (18)$$

The small constant $\epsilon > 0$ is typically introduced, to assure that the DICE is not undefined in case both segmentations are empty.

DISTS (Deep Image Structure and Texture Similarity)

Given the feature maps $F_l^i(I)$ and $F_l^i(R)$ from layer l and channel i of a pre-trained network, the structure similarity S_l^i and the texture similarity T_l^i between the feature maps were defined as

$$S_l^i(I, R) = \frac{2 \mu_{F_l^i(I)} \cdot \mu_{F_l^i(R)} + C_1}{\mu_{F_l^i(I)}^2 + \mu_{F_l^i(R)}^2 + C_1} \quad T_l^i(I, R) = \frac{2 \sigma_{F_l^i(I)} \cdot \sigma_{F_l^i(R)} + C_2}{\sigma_{F_l^i(I)}^2 + \sigma_{F_l^i(R)}^2 + C_2} \quad (19)$$

where C_1 and C_2 are positive constants. The overall DISTS metric is obtained by averaging weighted combinations of structure and texture similarities across network layers at different depths

$$\text{DISTS}(I, R) = \sqrt{\sum_l \sum_i (\alpha_l^i S_l^i(I, R) + \beta_l^i T_l^i(I, R))^2} \quad (20)$$

where α_l^i, β_l^i are optimized weighting factors for each channel i and layer l .

JNB (Just Noticeable Blur)

The idea of blurred edge widths (BEW) is extended with a notion of just noticeable blur. The image I is evaluated in smaller blocks b of size s_b . Only blocks $e \in \mathcal{E}$ with a sufficient fraction ($T > 0.002$) of edge pixels are considered. The edge widths are additionally weighted with the just noticeable blur width $\text{jnb}(e, L)$ depending on the maximal intensity range per block e and the data range L , which is 255 by default for 8-bit images. The exponential parameter $\beta = 3.6$ was also used for adjustments.

$$\mathcal{E} = \left\{ b \mid \frac{\sum_{\mathbf{x} \in b} \max_d E_d(\mathbf{x})}{s_b} > 0.002 \right\} \quad \text{jnb}(e, L) = \begin{cases} 5 & , \text{if } \frac{e_{\max} - e_{\min}}{L} \leq \frac{50}{255} \\ 3 & , \text{else} \end{cases} \quad (21)$$

$$\text{JNB}(I) = \frac{1}{|\mathcal{E}|} \cdot \sum_{e \in \mathcal{E}} \left(\sum_{\mathbf{x} \in e} \left(\frac{W_0(\mathbf{x})}{\text{jnb}(e, L)} \right)^\beta \right)^{1/\beta} \quad (22)$$

LPIPS (Learned Perceptual Image Patch Similarity)

The LPIPS metric extracts feature maps $F_l^i(I)$ and $F_l^i(R)$ from layer l and channel i of the pre-trained network. The feature maps are unit-scaled to $\hat{F}_l^i(I)$, $\hat{F}_l^i(R)$, weighted channel-wise with vectors w_l and subtracted. Then the corresponding L_2 norms are averaged spatially and summed to obtain the LPIPS distance $\text{LPIPS}(I, R)$:

$$\text{LPIPS}(I, R) = \sum_l \frac{1}{|F_l|} \sum_{\mathbf{x}_l} |w_l \odot (\hat{F}_l(I) - \hat{F}_l(R))(\mathbf{x}_l)|_2^2 \quad (23)$$

where \mathbf{x}_l denotes a pixel location in feature map F_l , \odot denotes the channel-wise multiplication and $|\cdot|_2$ denotes the euclidean norm. The linear weights w_l^i were optimized with the Berkeley-Adobe Perceptual Patch Similarity (BAPPS) Dataset [71].

MAE (Mean Absolute Error)

$$\text{MAE}(I, R) = \frac{1}{|I|} \sum_{\mathbf{x}} |R(\mathbf{x}) - I(\mathbf{x})| \quad (24)$$

MB (Mean Blur)

See the BR metric for details on how to compute the blurred edges B and the inverse blurriness IB . The MB metric is defined as the ratio of the summed inverse blurriness to the number of blurred pixels:

$$\text{MB} = \frac{\sum_{\mathbf{x}} \max_d IB_d(\mathbf{x})}{\sum_{\mathbf{x}} B(\mathbf{x})} \quad (25)$$

MLC (Mean Line Correlation)

The mean line correlation (MLC) metric is defined as the mean correlation between directly neighbored image lines:

$$\text{MLC} = \frac{1}{w} \sum_{x=1}^w \text{PCC}(I_c(x), I_c(x+1)) + \frac{1}{h} \sum_{y=1}^h \text{PCC}(I_r(y), I_r(y+1)) \quad (26)$$

MSE (Mean Squared Error)

$$\text{MSE}(I, R) = \frac{1}{|I|} \sum_{\mathbf{x}} (R(\mathbf{x}) - I(\mathbf{x}))^2 \quad (27)$$

MSLC (Mean Shifted Line Correlation)

The mean shifted line correlation (MSLC) metric is defined as the mean correlation between image lines, that are separated by $\lfloor w/2 \rfloor$ or $\lfloor h/2 \rfloor$ respectively.

$$\text{MLC} = \frac{1}{\lfloor w/2 \rfloor} \sum_{x=1}^{\lfloor w/2 \rfloor} \text{PCC}(I_c(x), I_c(x+1)) + \frac{1}{\lfloor h/2 \rfloor} \sum_{y=1}^{\lfloor h/2 \rfloor} \text{PCC}(I_r(y), I_r(y+1)) \quad (28)$$

MS-SSIM (Multi-Scale Structural Similarity Index Measure)

As for SSIM, luminance, contrast and structure are defined locally. For MS-SSIM they are calculated on different scales. Let I_M be the M -times low-pass filtered and downsampled version of image I . Then MS-SSIM is calculated locally as

$$\text{local-MS-SSIM}(I, R, \mathbf{x}) = l(I_M, R_M, \mathbf{x})^{\alpha_M} \cdot \prod_{j=1}^M c(I_j, R_j, \mathbf{x})^{\beta_j} \cdot s(I_j, R_j, \mathbf{x})^{\gamma_j} \quad (29)$$

where the weighting factors $\alpha_j = \beta_j = \gamma_j$ were determined experimentally for $j = 1 \dots 5$ as $[0.0448, 0.2856, 0.3001, 0.2363, 0.1333]$. Then the overall MS-SSIM value is averaged over all pixel locations:

$$\text{MS-SSIM}(I, R) = \frac{1}{|I|} \sum_{\mathbf{x} \in R} l(I_M, R_M, \mathbf{x})^{\alpha_M} \cdot \prod_{j=1}^M c(I_j, R_j, \mathbf{x})^{\beta_j} \cdot s(I_j, R_j, \mathbf{x})^{\gamma_j} \quad (30)$$

MTV (Mean Total Variation)

$$\text{MTV}(I) = \frac{1}{|I|} \sum_{\mathbf{x}} \sqrt{\sum_d (I(\mathbf{x}) - I(x_1, \dots, x_d + 1, \dots, x_n))^2} \quad (31)$$

NIQE (Natural Image Quality Evaluator)

The same 18 features are extracted as in the calculation of the BRISQUE metric. Additionally, The features are collected again on the image downsampled by factor two to obtain 36 features in total. This is done for all patches of size 96×96 in the image to be tested, and it was previously done for patches of reference training set consisting of undistorted natural images. The distribution of these features f_1, \dots, f_{36} can be fitted to a multivariate Gaussian model with mean ν and covariance matrix Σ . From patches of the reference dataset, ν_R and Σ_R were obtained. For any test image I , the fitted model parameters are denoted ν_I and Σ_I . The NIQE score is then defined as the difference between the fitted model parameters:

$$\text{NIQE}(I) = \sqrt{\left((\nu_R - \nu)^{-T} \cdot \left(\frac{\Sigma_R - \Sigma_I}{2} \right)^{-1} \cdot (\nu_R - \nu_I) \right)} \quad (32)$$

NMI (Normalized Mutual Information)

The joint probability distribution $p(I = i, R = r)$ represents the likelihood of pairs of intensity values $i = I(\mathbf{x})$ and $r = R(\mathbf{x})$ occurring at any pixel location \mathbf{x} in I and R . The joint probability distribution is computed by counting how many pixel locations x in I and R and dividing this number by the number of pixels $|I|$. Given an intensity $i \in [0, b - 1]$, the probability $p(I = i)$ is computed as the number of pixel locations \mathbf{x} with $I(\mathbf{x}) = i$ divided by the total number of pixels:

$$p(I = i) = \frac{|\{\mathbf{x} \mid I(\mathbf{x}) = i\}|}{|I|} \quad p(R = r) = \frac{|\{\mathbf{x} \mid R(\mathbf{x}) = r\}|}{|R|} \quad (33)$$

The Mutual information MI is then defined as

$$\text{MI}(I, R) = \sum_{i,r} p(I = i, R = r) \log \left(\frac{p(I = i, R = r)}{p(I = i)p(R = r)} \right) \quad (34)$$

where the sum is taken over all possible intensity values $i, r \in [0, b - 1]$ in the images I and R . MI can be expressed in terms of the entropy $H(I)$, $H(R)$ and $H(I, R)$ related the distributions $p(I)$, $p(R)$ and $p(I, R)$, respectively. We have:

$$\begin{aligned} H(I) &= - \sum_i p(I = i) \log p(I = i) & H(R) &= - \sum_r p(R = r) \log p(R = r) \\ H(I, R) &= - \sum_{i,r} p(I = i, R = r) \log p(I = i, R = r) & \text{MI}(I, R) &= H(I) + H(R) - H(I, R) \end{aligned} \quad (35)$$

The normalized mutual information (NMI) is defined as follows:

$$\text{NMI}(I, R) = \frac{\text{MI}(I, R)}{H(I, R)} + 1 = \frac{H(I) + H(R)}{H(I, R)} \quad (36)$$

NMSE (Normalized Mean Squared Error)

For images I and R , the normalized mean squared error is defined as

$$\text{NMSE}(I, R) = \frac{1}{|I| \cdot \sigma_R} \cdot \sum_{\mathbf{x}} (R(\mathbf{x}) - I(\mathbf{x}))^2 \quad (37)$$

where σ_R denotes the corrected sample standard deviation of the intensity value distribution of image R .

PCC (Pearson Correlation Coefficient)

$$\text{PCC}(I, R) = \frac{\sum_{\mathbf{x}} (I(\mathbf{x}) - \mu_I)(R(\mathbf{x}) - \mu_R)}{\sqrt{\sum_{\mathbf{x}} (I(\mathbf{x}) - \mu_I)^2} \sqrt{\sum_{\mathbf{x}} (R(\mathbf{x}) - \mu_R)^2}} \quad (38)$$

where the summations are taken over all pixel locations \mathbf{x} and $R(\mathbf{x})$, $I(\mathbf{x})$ denote the respective intensity values at that location.

PSNR (Peak Signal-to-Noise Ratio)

Please see MSE for the mean squared error.

$$\text{PSNR}(I, R) = 10 \cdot \log_{10} \left(\frac{L^2}{\text{MSE}(I, R)} \right) = 20 \cdot \log_{10}(L) - \log_{10}(\text{MSE}(I, R)) \quad (39)$$

RMSE (Root Mean Squared Error)

$$\text{RMSE}(I, R) = \sqrt{\frac{1}{|I|} \sum_{\mathbf{x}} (R(\mathbf{x}) - I(\mathbf{x}))^2} \quad (40)$$

SSIM (Structural Similarity Index Measure)

The structural similarity index measure (SSIM) combines local image luminance, contrast, and structure. Mean, standard deviation and covariance are calculated locally for each pixel location \mathbf{x} within a d -dimensional Gaussian kernel of size 11 and $\sigma = 1.5$ and are denoted by $\mu_I(\mathbf{x})$, $\sigma_I(\mathbf{x})$, $\mu_R(\mathbf{x})$, $\sigma_R(\mathbf{x})$ and $\sigma_{I,R}(\mathbf{x})$ respectively. For each pixel location \mathbf{x} and its local neighborhood in images I and R , the luminance l , contrast c and structure s are defined as:

$$\begin{aligned} l(I, R, \mathbf{x}) &= \left(\frac{2\sigma_I(\mathbf{x})\sigma_R(\mathbf{x}) + C_2}{\sigma_I(\mathbf{x})^2 + \sigma_R(\mathbf{x})^2 + C_2} \right)^\alpha \\ c(I, R, \mathbf{x}) &= \left(\frac{2\mu_I(\mathbf{x})\mu_R(\mathbf{x}) + C_1}{\mu_I(\mathbf{x})^2 + \mu_R(\mathbf{x})^2 + C_1} \right)^\beta \\ s(I, R, \mathbf{x}) &= \left(\frac{\sigma_{I,R}(\mathbf{x}) + C_3}{\sigma_I(\mathbf{x})\sigma_R(\mathbf{x}) + C_3} \right)^\gamma \end{aligned} \quad (41)$$

where C_1, C_2, C_3 are constants to avoid division by arbitrarily small numbers. The local luminance, contrast and structure are then multiplied and averaged for all pixel locations \mathbf{x} . Commonly, structure, luminance and contrast terms are weighted equally with $\alpha = \beta = \gamma = 1$. Choosing in addition $C_3 = C_2/2$ yields a simplified formula:

$$\text{SSIM}(I, R) = \frac{1}{|I|} \sum_{\mathbf{x} \in I} \frac{(2\mu_I(\mathbf{x})\mu_R(\mathbf{x}) + C_1) \cdot (2\sigma_{I,R}(\mathbf{x}) + C_2)}{(\mu_I(\mathbf{x})^2 + \mu_R(\mathbf{x})^2 + C_1) + (\sigma_I(\mathbf{x})^2 + \sigma_R(\mathbf{x})^2 + C_2)} \quad (42)$$

The other constants are commonly selected as $C_1 = (0.01 \cdot L)^2$ and $C_2 = (0.03 \cdot L)^2$ with $L = 255$ defined as the data range of the intensity values, in the common case of 8-bit unsigned integers, $L = 255$ [65], otherwise $L = \max(I_{\max}, R_{\max}) - \min(I_{\min}, R_{\min})$. See also CW-SSIM and MS-SSIM.

VL (Variance of Laplacian)

The Laplacian of an image I can be calculated by convolution (*) with the Laplacian filter:

$$\text{Laplace}(I) = I * \begin{pmatrix} 0 & 1 & 0 \\ 1 & -4 & 1 \\ 0 & 1 & 0 \end{pmatrix} \quad (43)$$

Then, the variance is calculated:

$$\text{VL}(I) = \frac{1}{|I|} \sum_{\mathbf{x} \in I} (\text{Laplace}(I)(\mathbf{x}) - \mu_{\text{Laplace}(I)})^2 \quad (44)$$

A.4 Calculation of Distortions

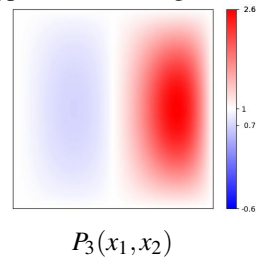
For each type of distortion, the range of parameters is given for strengths $s = 1$ to $s = 5$. All other strengths are interpolated linearly between the given values. The distorted image is denoted as \tilde{I} . Let $\mathbf{s} = (w, h)$ be the image size vector of I . The minimum and maximum intensity of I are denoted by I_{\min}, I_{\max} . Inverted transformations, that can restore a transformed image, are denoted by $^{-1}$, e.g. Minmax $^{-1}$, FFT $^{-1}$ or shift $^{-1}$. Distortions are ordered alphabetically.

Bias Field, $c \in [0.5, 10]$

An artificial bias field is created from the polynomial function P_3 and applied to the image:

$$P_3(x_1, x_2) = 10x_1^2(x_1 - 1) \cdot (x_2 - 0.5)x_2(x_2 - 1) \quad (45)$$

$$\tilde{I} = I \cdot e^{c \cdot P_3}$$



Elastic Deform, $n \in [18, 11], d \in [0.03, 0.1]$

A grid with n^2 points is created, and points are displaced by a displacement vector sampled from $\mathcal{N}(\mu = \mathbf{0}; \sigma = d \cdot \frac{s}{n})$. The image is interpolated along the grid.

Gamma Low / Gamma High, $\log(\gamma) \in [-0.01, -0.916] / \log(\gamma) \in [0.095, 0.916]$

$$\tilde{I} = \text{Minmax}^{-1}(\text{Minmax}(I)^\gamma) \quad (46)$$

Gaussian Blur, $\sigma \in [0.2, 1.3]$

The image is convoluted with a Gaussian kernel G_σ :

$$\tilde{I} = \text{Conv}(G_\sigma, I) \quad (47)$$

Gaussian Noise, $\sigma \in [0.005, 0.05]$

$$\tilde{I} = I + \mathcal{N}(\mu = 0; \sigma) \quad (48)$$

Ghosting, $i \in [0.05, 0.4]$

The fast Fourier transform (FFT) transforms the image to the frequency domain. The shift operator then moves the center of the transformed image to 0. The spectrum is scaled (distorted) at every second pixel (to generate two ghosts) along the first axis, then the image is restored for all pixels with $x_1 = w/2$.

$$\begin{aligned} I' &= \text{shift}(\text{FFT}(I)) \\ I''(x_1, x_2) &= I' \cdot i, \text{ for } x_1 \% 2 = 0 \\ I''(x_1, x_2) &= I', \text{ for } x_1 = w/2 \\ \tilde{I} &= \text{shift}^{-1}(\text{FFT}^{-1}(I'')) \end{aligned} \quad (49)$$

Replace Artifact, $f \in [0.1, 1.0]$

Copy and mirror a fraction of the upper half of the image to the lower half:

$$\tilde{I}(x_1, x_2) = \begin{cases} I(x_1, x_2) & , \text{if } x_2 \leq \frac{h}{2} \\ I(x_1, h - x_2) & , \text{if } x_2 > \frac{h \cdot (1+f)}{2} \end{cases} \quad (50)$$

Shift Intensity, $f \in [0.05, 0.25]$

$$\tilde{I} = I + f \cdot (I_{\max} - I_{\min}) \quad (51)$$

Stripe Artifact, $i \in [0.05, 0.5]$

The fast Fourier transform (FFT) transforms the image to the frequency domain. The shift operator then moves the center of the transformed image to 0. The spectrum is scaled (distorted) at a single pixel $(0.3 \cdot \cos(0), 0.3 \cdot \sin(0))$. Then the image is transformed back to the spatial domain again.

$$\begin{aligned} I' &= \text{FFT}(\text{shift}(I)) \\ I''(x_1, x_2) &= i \cdot I_{\max}, \text{ for } x_1 = 0.3 \cdot \cos(0), x_2 = 0.3 \cdot \sin(0) \\ \tilde{I} &= \text{FFT}^{-1}(\text{shift}^{-1}(I'')) \end{aligned} \quad (52)$$

Translation, $f \in [0.01, 0.2]$

$$\tilde{I}(x_1, x_2) = I(f \cdot w + x_1, f \cdot h + x_2) \quad (53)$$

B All Result Plots

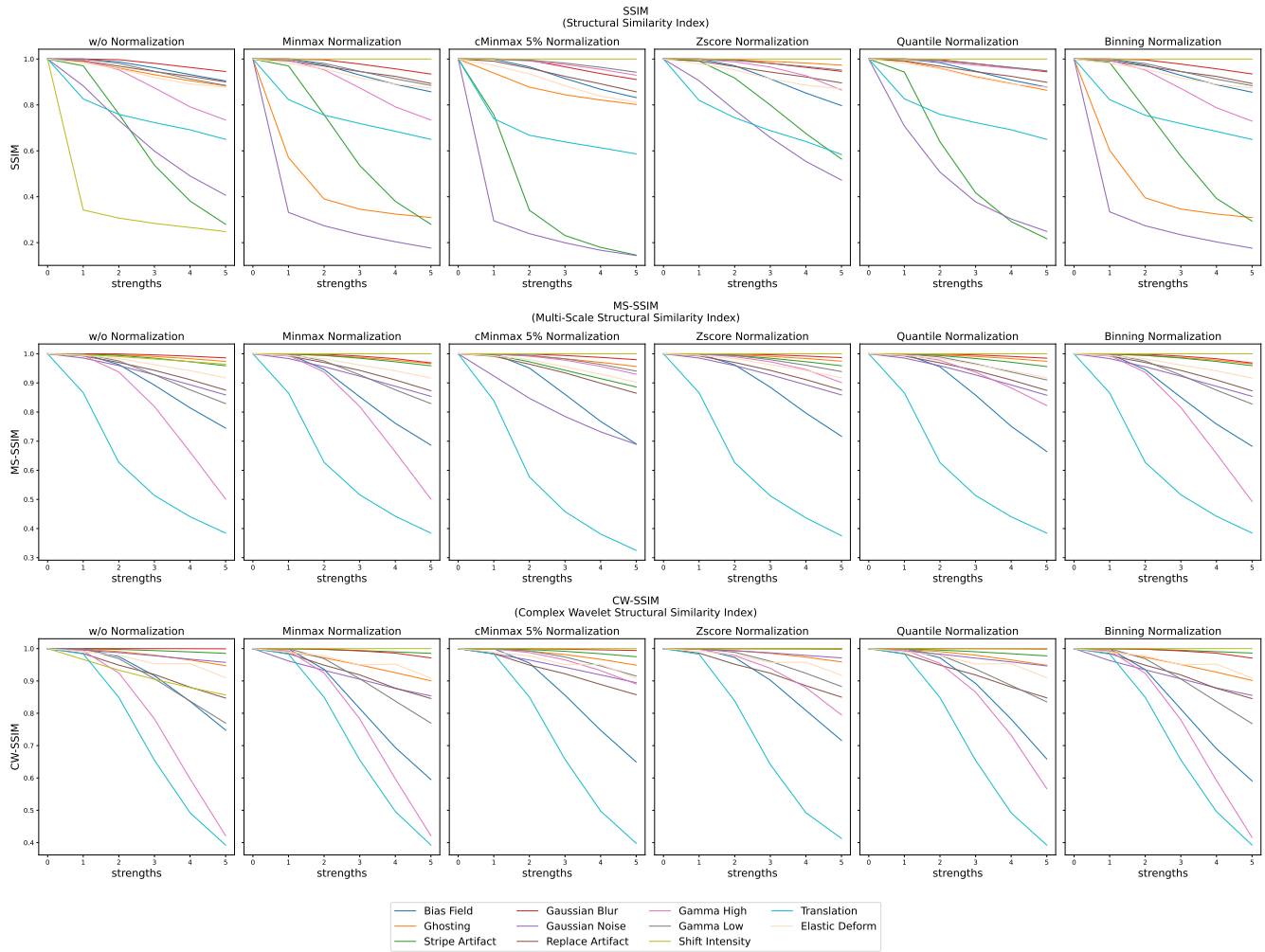


Figure S.3. Median scores of SSIM-based reference metrics SSIM (top), MS-SSIM (middle), and CW-SSIM (bottom) across 100 images, distorted with increasing strengths (0: reference, 1: hardly/not visibly distorted, 5: strongly distorted), grouped by kinds of distortions in different colors.

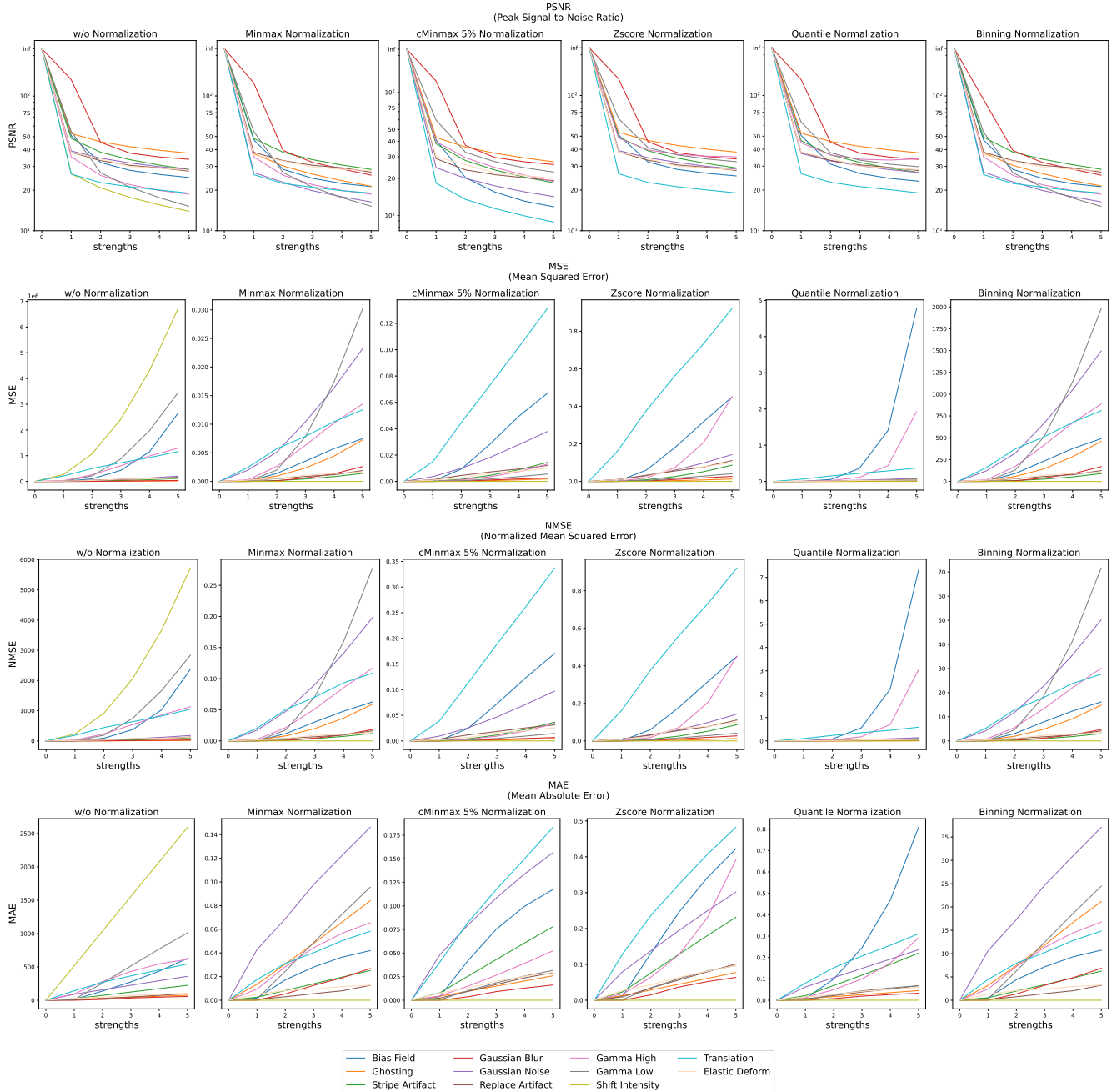


Figure S.4. Median scores of error-based reference metrics PSNR (top), MSE (second row), NMSE (third row) and MAE (bottom) across 100 images, distorted with increasing strengths (0: reference, 1: hardly/not visibly distorted, 5: strongly distorted), grouped by kinds of distortions in different colors.

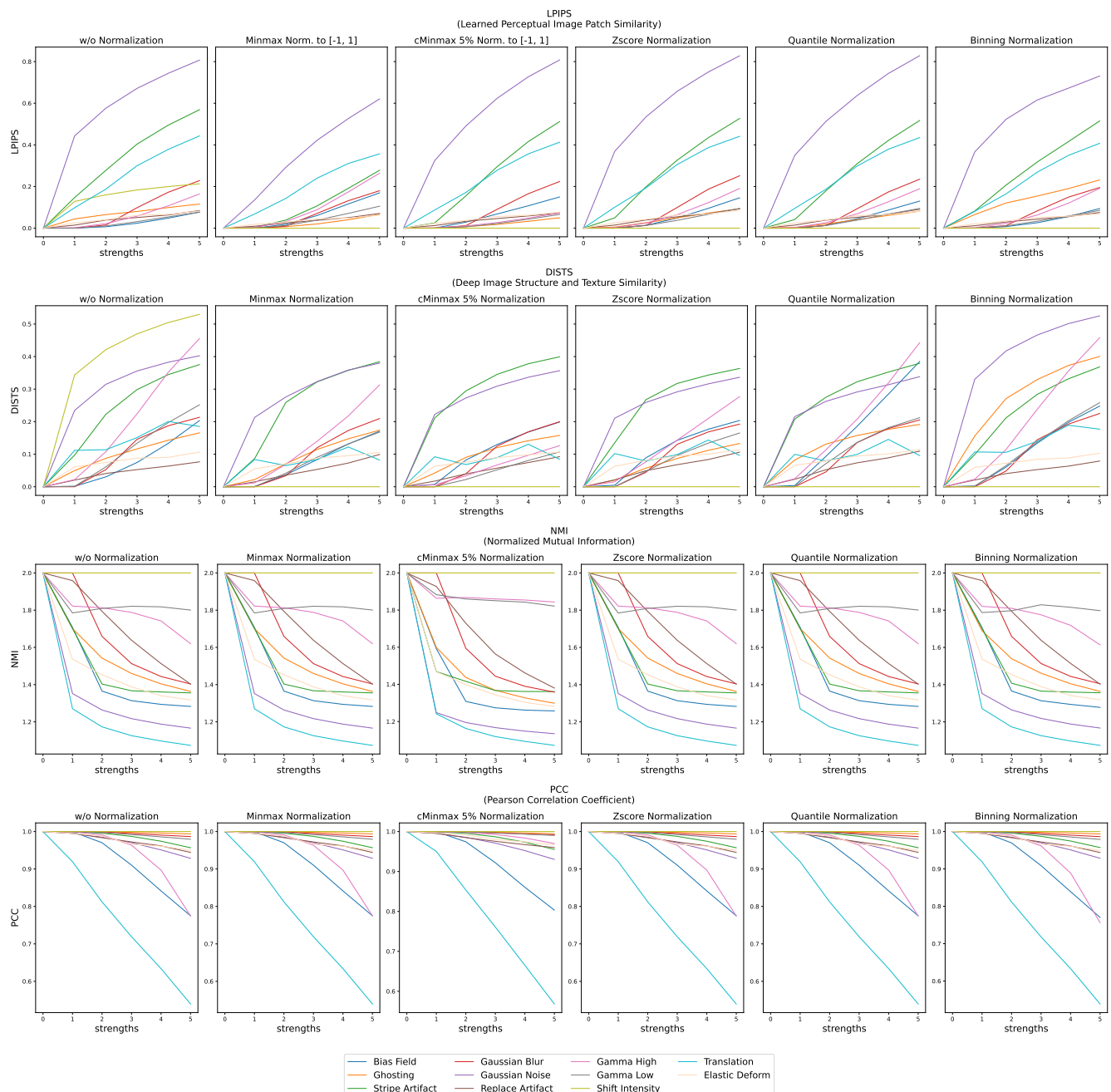


Figure S.5. Median scores of the learned reference metrics LPIPS (top) and DISTs (second row), and statistical dependency reference metrics NMI (third row) and PCC (bottom) across 100 images, distorted with increasing strengths (0: reference, 1: hardly/not visibly distorted, 5: strongly distorted), grouped by kinds of distortions in different colors. LPIPS and DISTs require normalized images with an intensity range around 0, therefore, analysis of these metrics was not performed without normalization.

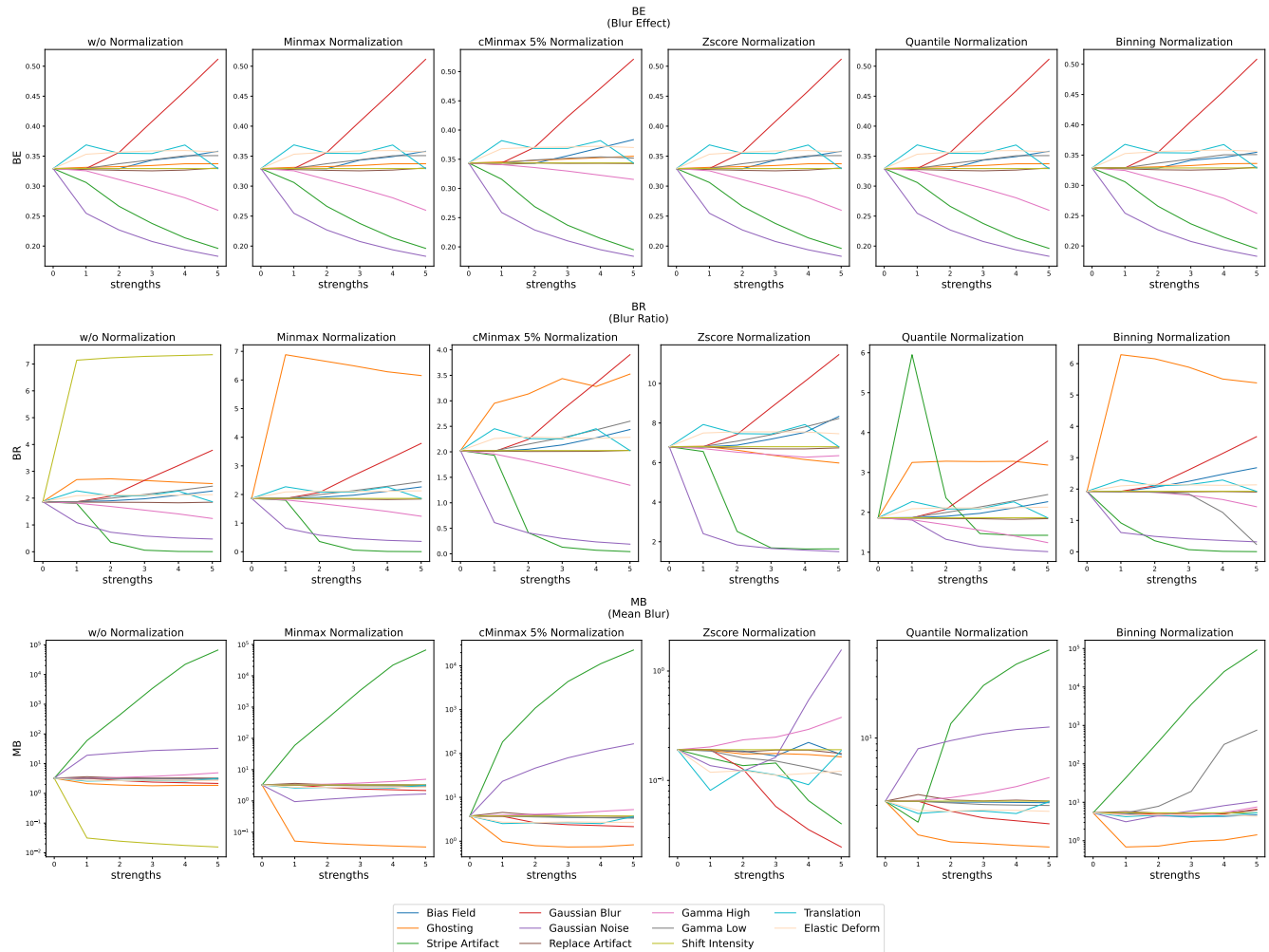


Figure S.6. Median scores of non-reference blurriness metrics BE (top), BR (middle) and MB (bottom) across 100 images, distorted with increasing strengths (0: reference, 1: hardly/not visibly distorted, 5: strongly distorted), grouped by kinds of distortions in different colors.

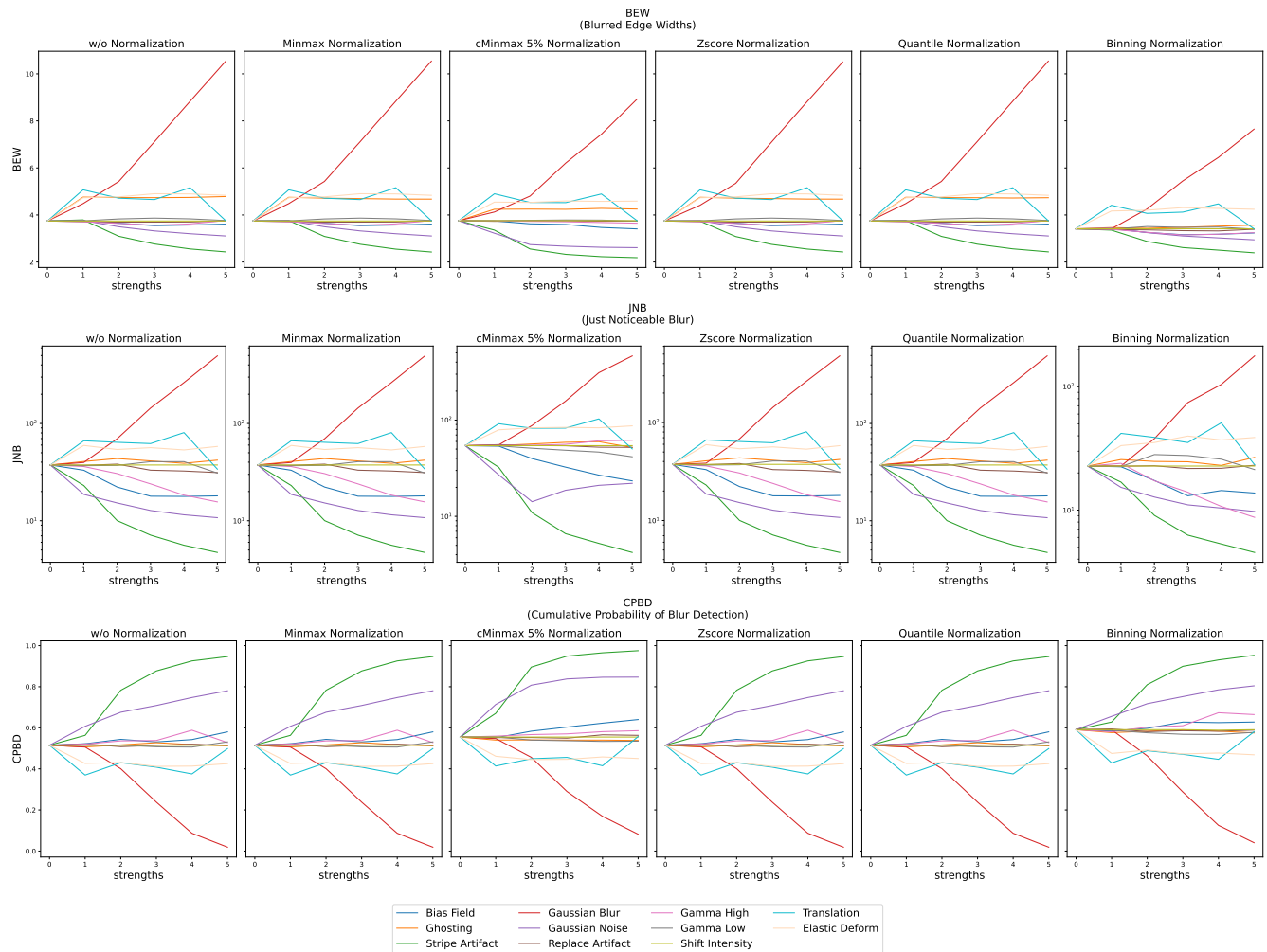


Figure S.7. Median scores of non-reference blurriness metrics BEW (top), JNB (middle) and CPBD (bottom) across 100 images, distorted with increasing strengths (0: reference, 1: hardly/not visibly distorted, 5: strongly distorted), grouped by kinds of distortions in different colors.

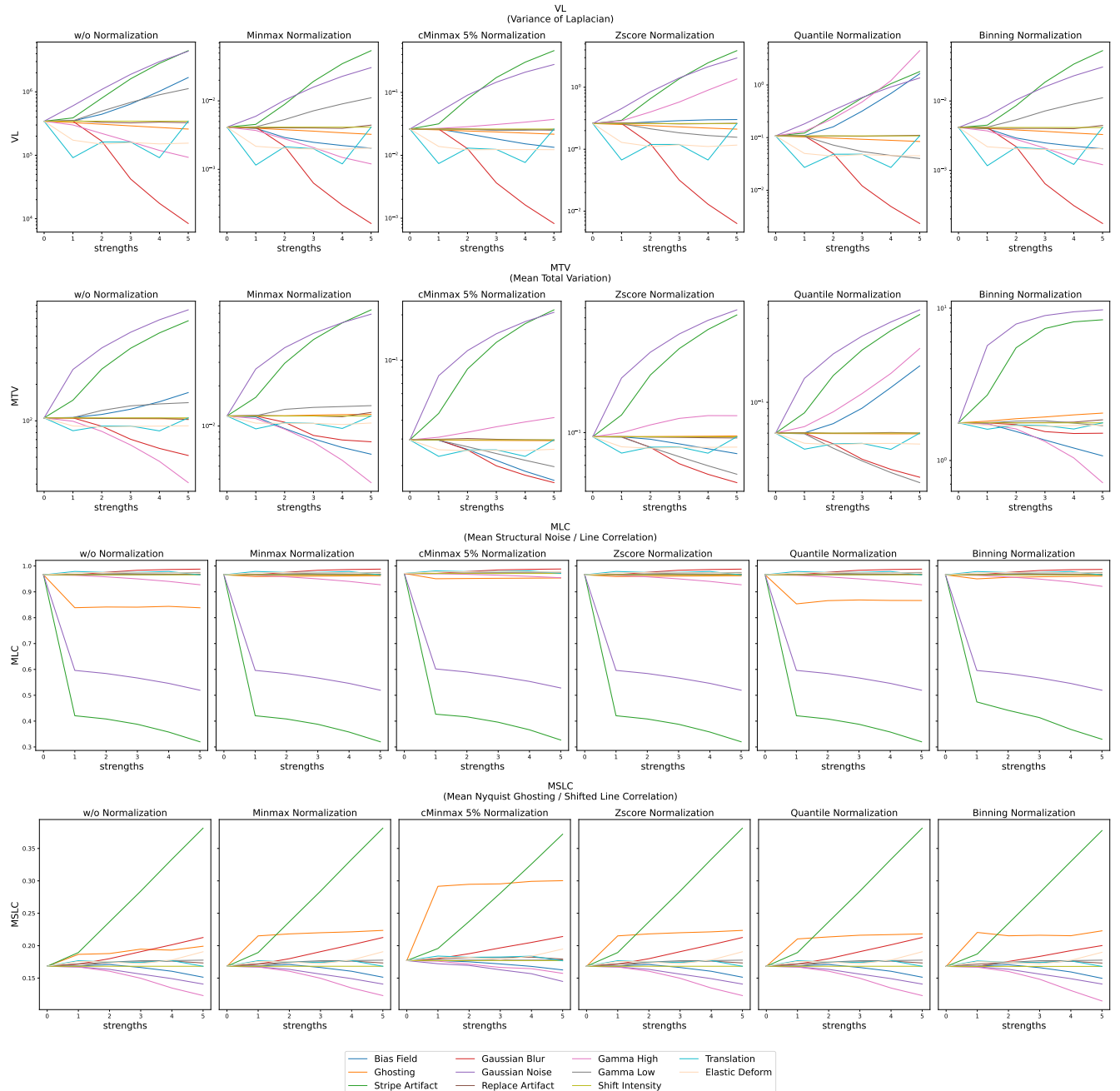


Figure S.8. Median scores of further non-reference blurriness, noisiness and MR acquisition quality metrics VP (top), MTV (second row), MLC (third row), and MSLC (bottom) metric across 100 images, distorted with increasing strengths (0: reference, 1: hardly/not visibly distorted, 5: strongly distorted), grouped by kinds of distortions in different colors.

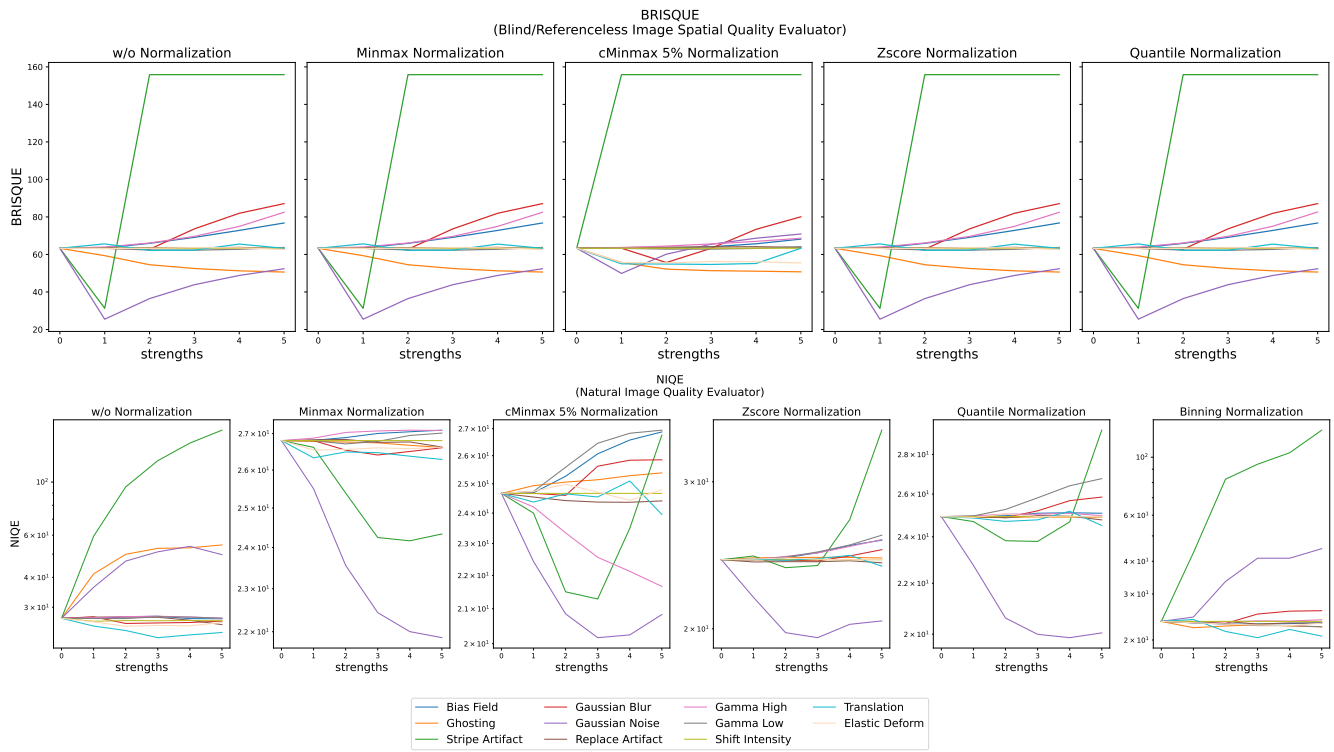


Figure S.9. Median scores of the learned non-reference quality metrics BRISQUE (top), and NIQE (bottom) metric across 100 images, distorted with increasing strengths (0: reference, 1: hardly/not visibly distorted, 5: strongly distorted), grouped by kinds of distortions in different colors.

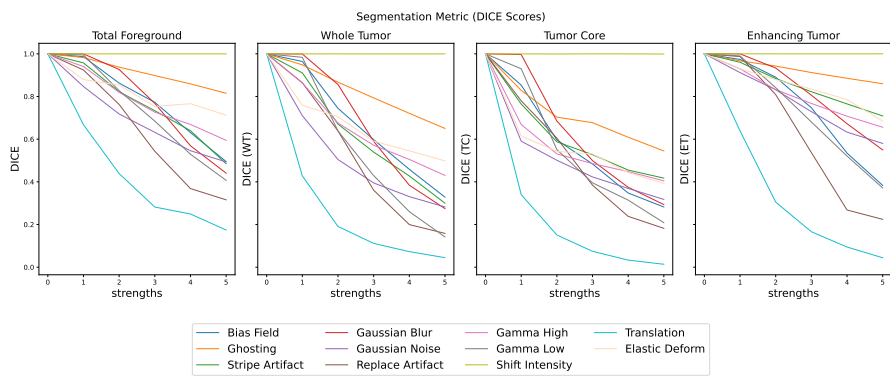


Figure S.10. Mean scores of the DICE segmentation metric across 100 segmentation pairs derived from a reference a distorted image with increasing strengths applied (0: reference, 1: hardly/not visibly distorted, 5: strongly distorted). The mean scores are grouped by kinds of distortions in different colors. The "Total Foreground" class includes the three disjoint classes "Whole Tumor" (mainly tumor surrounding edema), "Tumor Core" (mainly necrotic areas) and "Enhancing Tumor" (vital tumor cells, taking up contrast media).